

Student thesis series INES nr 546

Exploring Spatiotemporal Relationships between InSAR-derived Land Subsidence and Satellite-based Hydrological Variables

Yixin Zhang

2021
Department of
Physical Geography and Ecosystem Science
Lund University
Sölvegatan 12
S-223 62 Lund
Sweden



Yixin Zhang (2021).

Exploring Spatiotemporal Relationships between InSAR-derived Land Subsidence and Satellite-based Hydrological Variables

Master degree thesis, 30 credits in *Geomatics*

Department of Physical Geography and Ecosystem Science, Lund University

Level: Master of Science (MSc)

Course duration: *January* 2021 until *June* 2021

Disclaimer

This document describes work undertaken as part of a program of study at the University of Lund. All views and opinions expressed herein remain the sole responsibility of the author, and do not necessarily represent those of the institute.

Exploring Spatiotemporal Relationships between InSAR-derived Land Subsidence and Satellite-based Hydrological Variables

Yixin Zhang

Master thesis, 30 credits, in *Geomatics*

Supervisor:

Hossein Hashemi

Department of Water Resources Engineering and Center for Advanced
Middle Eastern Studies, Lund University, Sweden

Exam committee:

Zheng Duan

Mitro Müller

Department of Physical Geography and Ecosystem Science, Lund
University, Sweden

Acknowledgments

I would like to express my deepest gratitude to my supervisor Hossein Hashemi at the Department of Water Resources Engineering and Center for Advanced Middle Eastern Studies, for providing me with the opportunity of working on this research topic. I would like to thank him for his expertise, feedback, time, encouragement, and overall insights in this field. I would like to thank Seyed Amir Naghibi and Behshid Khodaei in Hossein Hashemi's group for their valuable suggestions, motivation, and time.

I would also like to thank Lund University for letting me fulfill my dream of being a student here. I really enjoy my time in Lund during my undergraduate and graduate studies. Thanks Lund University and the department for giving me the opportunity to explore more, be more fearless, and be a better me.

I would like to thank my friends in Lund, Wuhan, Beijing, and Xiamen, who help me survive the stress from this year.

Finally, I would like to express my deep and sincere gratitude to my family, especially my parents, for their mental and emotional support, patience, and love. They kept me going, and this thesis would not have been possible without them in this tough year. I would also like to thank myself for trying without giving up.

Abstract

Shabestar basin in the East Azerbaijan province, Northwest Iran, where irrigation is the main groundwater consumer, has experienced large-scale subsidence and groundwater depletion, which poses a threat to the local agricultural activities, economic development, and food security. With the emergency of mitigating the risk, satisfying future demand for groundwater, and improving resilience considering climate change, this study proposes a satellite-based approach to explore the spatio-temporal relationships between measured subsidence and hydrological variables in the basin to assist groundwater management strategy.

We investigated ground subsidence in the basin using the SBAS-InSAR technique based on series of Sentinel-1A TOPS Synthetic Aperture Radar (SAR) images acquired from 22 January 2016 to 21 October 2020 along ascending and descending tracks. The study showed average subsidence rates ranged from -97.5 mm/year to 10 mm/year in the basin after decomposing line-of-sight velocity fields to vertical components. The prominent subsidence was found in the eastern and western portions of the basin, and the maximum average subsidence rate was detected in the eastern part of the basin near Nazarlu.

Correlation analysis between the surface subsidence and potential driving factors, including the actual evapotranspiration (ET_a), land surface temperature (LST), the normalized difference vegetation index (NDVI), precipitation (P), and soil water index (SWI), revealed a significant relationship between the first three variables and observed subsidence by InSAR. A multivariate long short-term memory (LSTM) network was established to investigate the importance of the first three variables and predict subsidence in the near future. The result quantitatively revealed that the agricultural practice had a major impact on subsidence occurrence in the basin. Furthermore, our findings indicated that the area is estimated to continue subsiding dramatically in the next five years. This study fills the gap in the local groundwater monitoring system using satellite-based data and artificial intelligence and contributes to the local groundwater management by providing insights into the main drivers of groundwater-induced subsidence.

Keywords: InSAR, Shabestar, subsidence, groundwater, hydrological variables, LSTM, Sentinel-1A

Table of Contents

List of Abbreviations	I
List of Figures.....	II
List of Tables.....	III
1. Introduction	1
1.1 Aim and research questions	2
2. Background.....	3
2.1 Theory of InSAR technique.....	3
2.1.1 Principles of Synthetic Aperture Radar.....	3
2.1.2 InSAR principles.....	5
2.1.3 Small Baseline Subset (SBAS) technique.....	8
2.2 Potential proxies for land subsidence	9
2.3 Study area	10
2.3.1 Geological and hydrogeological setting.....	11
2.3.2 Related study.....	12
3. Data and Methodology	13
3.1 SBAS-InSAR-derived deformation.....	13
3.1.1 Data used.....	13
3.1.2 Data processing	14
3.2 Hydrological variables and deep learning methods	17
3.2.1 Data used.....	17
3.2.2 Data interpolation and harmonization.....	21
3.2.3 Time lag	23
3.2.4 Multivariate Long short-term memory (LSTM) modeling.....	25
4. Result	28
4.1 InSAR-derived deformation	28
4.2 Lag correlation	31
4.3 Model evaluation and variable importance	35
4.4 Model prediction	38
5. Discussion	39
5.1 Spatial and temporal analysis	39
5.2 Data	41
5.3 Model.....	42
5.4 Future groundwater management.....	43

6. Conclusion	44
7. Reference	45
Appendix	51

List of Abbreviations

CGLS	Copernicus Global Land Service
CHRS	Center for Hydrometeorology and Remote Sensing
DEM	Digital Elevation Model
Detrend VD	Detrend Vertical Displacement
EEFlux	Earth Engine Evapotranspiration Flux engine
EO	Earth Observation
ESA	European Space Agency
ETa	Actual Evapotranspiration
GEE	Google Earth Engine
InSAR	Interferometric Synthetic Aperture Radar
IW	Interferometric Wide Swath
LOS	Line-Of-Sight
LST	Land Surface Temperature
LSTM	Long Short-Term Memory
mm	millimeters
MSE	Mean Square Error
NDVI	The Normalized Difference Vegetation Index
P	Precipitation
PERSIANN-CCS	PERSIANN-Cloud Classification System
POD	Precise Orbit Determination
RMSE	Root Mean Square Error
SAR	Synthetic Aperture Radar
SBAS	Small Baseline Subset
SBAS-InSAR	Small Baseline Subset InSAR
SHAP	SHapley Additive exPlanations
SLAR	Side-looking Airborne Radar
SLC	Single Look Complex
SNAPHU	Statistical-cost Network-flow Phase-unwrapping algorithm
SRTM	Shuttle Radar Topography Mission
SWI	Soil Water Index
TOPSAR	Terrain Observation with Progressive Scans SAR
2D	Two dimensional
3D	Three dimensional

List of Figures

Figure 1. Concept diagram of a side-looking radar satellite.....	4
Figure 2. The geometry of InSAR investigations configurations.....	6
Figure 3. The geological map of the study area.	12
Figure 4. Temporal and perpendicular baselines of Sentinel-1A images interferometric pairs from ascending (4a) and descending (4b) tracks.	15
Figure 5. Concept diagram of a 3D array for image interpolation	22
Figure 6. Concept diagram of the LSTM cells	25
Figure 7. Concept diagram of an LSTM model.....	26
Figure 8. (a) Line-of-sight (LOS) velocity maps derived from Sentinel-1A ascending orbits; and (b) LOS velocity maps from Sentinel-1A descending track.	29
Figure 9. Comparison of mean LOS deformation velocity between ascending and descending orbits. a) Correlation between the LOS deformation rates from the two different datasets. b) Difference analysis between the ascending and descending tracks.	30
Figure 10. Spatial pattern of mean velocity in a vertical direction from ascending (a) and descending (b) data sets.	31
Figure 11. Vertical displacement time series for five zones.	34
Figure 12. Average values at each date for each variable in Zone 1. Time shifts for five variables (ETa, LST, NDVI, P, and SWI) were applied.	34
Figure 13. Loss function plots.....	35
Figure 14. Test dataset vs. predicted values with RMSE values for each zone over time.....	36
Figure 15. Variable importance charts for each zone created using the SHAP package in Python.	37
Figure 16. Actual and predicted vertical displacement over the studied time span for each zone.....	38
Figure S1. Average values at each date for each variable in Zone 2, 3, 4, and 5. Time shifts for five variables (ETa, LST, NDVI, P, and SWI) were applied.	51

List of Tables

Table 1. Description of Sentinel-1A images from both tracks.....	14
Table 2. Description of satellite-based hydrological variables.....	19
Table 3. Maximum correlation coefficient within a 300-day time frame between the five variables and detrended subsidence time series in five zones during the study period. .	32
Table 4. Maximum correlation coefficient within a 300-day time frame between the five variables and detrended subsidence time series in five zones during the study period. .	33

1. Introduction

Groundwater aquifers hold over 98% of the global freshwater resources to supply agricultural, domestic, and industrial water worldwide (Velis et al. 2017). Long-term groundwater overexploitation leads to groundwater depletion and contamination, land subsidence, and seawater intrusion. Overexploitation of such nonrenewable resources results in water scarcity and the compaction of fine-grained materials, consequently observed as subsidence on the ground surface, which poses a threat to public safety. One-third of the global largest groundwater basin experienced dramatic depletion ascribed to human consumption in the last few decades (Richey et al. 2015a, 2015b). Additionally, the potential groundwater depletion in many regions is still unknown (Scanlon et al. 2016). Recent climate change and growing water demands aggravate the problem, especially in arid and semi-arid regions, caused by population growth, agricultural area expansion, and economic development (Döll 2009; Ferrant 2014). Therefore, it is crucial to innovate new and economical groundwater monitoring systems to assist groundwater management and enhance resilience in the face of rising water demand and climate change.

NASA's Gravity Recovery and Climate Experiment (GRACE) satellite data are used to evaluate groundwater storage dynamics to address gaps in groundwater monitoring systems (Rodell et al. 2007; Scanlon et al. 2012; Döll et al. 2014; Xiang et al. 2016). However, the technique, limited by the spatial resolution of GRACE data (300–400 km), is not appropriate for monitoring variations in groundwater levels at local scales (Castellazzi et al. 2016). Interferometric Synthetic Aperture Radar (InSAR) provides ground deformation measurements with millimeter-to-centimeter- accuracy and a high spatial resolution of approximately 20 to 100 m over different time intervals. While the traditional method requires a large number of in-site measurements to, i.e., build and calibrate a groundwater model, the aquifer characterization and groundwater level dynamics can be estimated at basin scales by combining InSAR-derived deformation timeseries and local observation of groundwater levels (Hoffmann et al. 2001, 2003; Chaussard et al. 2014; Béjar-Pizarro et al. 2017; Chen et al. 2017; Jiang et al. 2018; Ojha et al. 2018). To date, few studies have utilized the InSAR technique in areas with limited in-site data to assist groundwater management. In this project, taking advantage of the InSAR technique and multiple satellite-based data, we explore the

relationships between InSAR-derived deformations and satellite-based hydrological variables, spatially and temporally, to assist groundwater management strategy.

Because irrigation is one of the primary groundwater consumers, we are interested in measuring land deformation in vegetated regions using the InSAR technique and identify the subsidence driving factors in the agricultural areas. Shabestar basin that is located in East Azerbaijan Province, Iran, and bordered by the Urmia Lake, is an ideal location to monitor land surface deformation. The majority of the basin is covered by agricultural land highly dependent on the groundwater resource (Zeinali et al. 2010; EARWA 2015).

A challenge of using InSAR to derive land subsidence over agricultural land is that InSAR phase measurements may be affected by signal decorrelation attributed to vegetation growth. Small Baseline Subset (SBAS) InSAR approach can mitigate phase decorrelation effects by using the interference of multiple pairs of master images and analyzing the high-coherence points (Ferretti et al. 2000; 2001). In this study, we first derive land deformation using the SBAS-InSAR technique, identified the subsidence driving hydrological factors, and predict land subsidence in near future in the study area using gridded hydrological variables and a deep learning framework to contribute to the local groundwater management.

1.1. Aim and research questions

The objectives of this study are: 1) Investigate spatiotemporal vertical ground deformation using multitemporal Sentinel-1A ascending data from 2016-2020 based on the InSAR technique; 2) Validate the InSAR deformation map by processing the Sentinel-1A from the descending track; and 3) Explore a new satellite-based method with InSAR-derived land surface displacements and deep learning to inform groundwater management.

Three main specific research questions are:

1. How can the SBAS InSAR technique be used to generate the ground deformation?
2. How well are the InSAR-derived vertical surface displacements?
3. How to associate satellite-based hydrological variables to the InSAR-derived ground deformation data to inform groundwater management strategy?

2. Background

2.1 Theory of InSAR technique

2.1.1. Principles of Synthetic Aperture Radar

Radar-based systems can penetrate cloud cover and vegetation and be independent of solar radiation. The systems have a distinct advantage of providing 24-hour all-weather Earth Observation (Oliver and Quegan 2004). The origin of Synthetic Aperture Radar (SAR) satellites is side-looking airborne radar (SLAR). SLAR system was developed in the 1950s. Unlike optical imaging systems, which point directly downward (nadir), the satellite of a SLAR system moves forward along its track with looking away from nadir by a look angle which defines the line-of-sight (LOS) of the acquisition. The antenna of the system transmits microwave pulses in this side-looking direction towards the ground to illuminate a swath on the Earth's surface. The swath is called the antenna footprint (Figure 1). The spatial resolution of the antenna footprint is computed in the along-track (azimuth) direction and the across-track (range) direction. The range resolution is dependent on the length of the pulses. The azimuthal resolution is determined by the beamwidth, which is inversely proportional to the antenna's length. A longer antenna produces a narrower beam and a finer resolution in the azimuth direction. As an advanced SLAR system, a SAR system simulates a long antenna by synthesizing a sequence of radar echoes that are generated by the movement of the satellite to form high-resolution imagery (Moreira et al. 2013).

SAR systems operate at different wavelengths (Committee on Earth Observation Satellites [CEOS] 2018), which are referred to as bands, e.g., C-band (7.5-3.8cm), L-band (30-15cm), and P-band (100-30cm). Different wavelengths have different penetrating capacities and ways of interacting with the ground. For example, the longer wavelength in L-band is characterized by a greater penetration capability for targets like dense canopy covers, ice, and sand, in contrast to the shorter wavelength in C- and X-band. However, an L-band image has a lower resolution than C- and X-band image because of its small bandwidth.

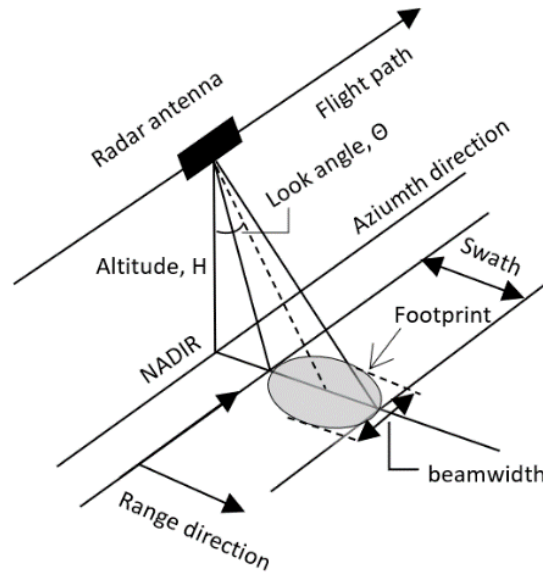


Figure 1. Concept diagram of a side-looking radar satellite. © Yixin Zhang (2021)

The antenna of the SAR satellite sends electromagnetic waves towards the ground and receives the proportion of reflected echoes from the surface. Reflected echoes are also called backscattered signals. The amplitude and phase of these backscattered signals are recorded as a function of time in SAR imagery. The amplitude is a measure of the magnitude of the reflected signal. The brightness of ground features in an amplitude image is dependent on the strength of the backscattered energy, and the backscatter intensity is dependent on how signals interact with the ground features. For example, a rough surface that scatters energy in all directions appears bright in the image because it has a considerably high backscatter intensity. Phase value reveals the timing of a point within a wave cycle of a repeating waveform. Scatters, which have different slant ranges from the antenna, generate different delay times between transmission and reception of signals. Because the transmitted signal is almost a sinusoidal waveform, a phase change ϕ can then be used to estimate the delay τ . The phase difference ($\Delta\phi$) between two periodic signals is proportional to wavelength as:

$$\Delta\phi = \frac{2\pi}{\lambda} \times (\text{path difference}) \quad \text{Eq. 1}$$

When a radar antenna transmits and receives electromagnetic waves, the direction of the electric field vector or the orientation of the polarization is always perpendicular to its magnetic field. SAR systems can capture information on the physical properties of the observed target by changing the polarization of the sending signals. SAR

systems are single-polarized or dual-polarized (CEOS 2018). A single-polarization system transmits and receives waves in the same direction; A dual-polarization system transmits waves in one polarization and receives in two polarizations. A fully polarimetric SAR system can have four polarization configurations: a horizontal-horizontal (HH), a vertical-vertical (VV), a horizontal-vertical (HV), or a vertical-horizontal (VH).

2.1.2. InSAR principles

SAR Interferometry (InSAR) is a radar technique for generating Digital Elevation Models (DEM) and mapping centimetric land surface deformations by measuring the phase difference between two coherent SAR images (Zebker et al. 1994; Rosen et al. 2000; Ferretti et al. 2001). A complex image or a complex interferogram can be generated by a cross-multiplication between the first image (the master) and the complex conjugate of the second (the slave), pixel by pixel (Bamler and Hartl 1998; Rosen et al. 2000). Thus, the interferograms contain information about the multiplication of amplitude and the phase difference between the two SAR images. Methods for obtaining two interfering SAR images can be classified based on the relative positions of antennas as the following two concepts (Moreira et al. 2013), i) across-track interferometry; and ii) along-track interferometry.

The first method is based on one or two satellites that are space-separated along the across-track direction. The configuration acquires the two SAR images from different orbital positions at different times (repeat-pass interferometry) or from different positions at the same time (single-pass interferometry). The second approach uses two sensing antennas that are spatially separated in the along-track direction. The image pairs are acquired from two satellites over the same area at different times. The concept of InSAR investigations configurations is indicated in Figure 2.

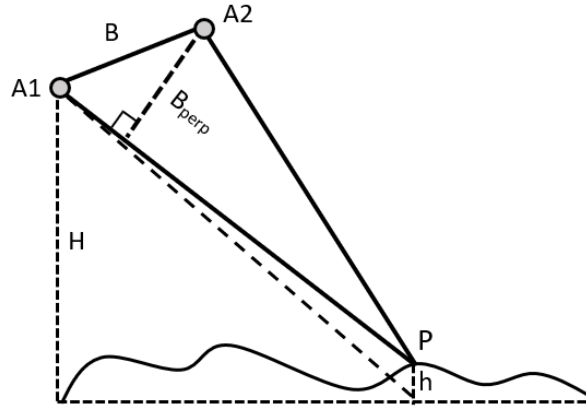


Figure 2. The geometry of InSAR investigations configurations. The distance between two acquisitions is called interferometer baseline (B). The perpendicular distance between two acquisitions is called perpendicular baseline (B_{perp}). $A1$ and $A2$ is the position of master and slave acquisition, respectively. P is the point of the ground target. h is the topographic height of the point. H is the height of the satellite. © Yixin Zhang (2021)

2.1.2.1. Phase Coherence

Coherence γ , which is also called the complex correlation coefficient, plays an important role in explaining the precision of the interferogram. The value provides information about the properties of scatters. A higher coherence value reveals less noise in the interferogram and more reliable results. The expression of the coherence γ is shown below (Rosen et al. 2000):

$$\gamma = \frac{E[s_1 \cdot s_2^*]}{\sqrt{E[s_1^2]E[s_2^2]}}; |\gamma| < 1 \quad \text{Eq. 2}$$

where E is the expected values of x ; s_1 and s_2 are the two complex images. $*$ means a complex conjugate product.

The coherence of the interferogram is mainly affected by six following decorrelation variables which will reduce the quality of the interferogram (Zebker and Villasenor 1992; Bamler and Hartl 1998):

$$\gamma_{total} = \gamma_{temporal} \cdot \gamma_{geo} \cdot \gamma_{DC} \cdot \gamma_{vol} \cdot \gamma_{noise} \cdot \gamma_{pro} \quad \text{Eq. 3}$$

- a) $\gamma_{temporal}$: changes in scattering properties due to the natural changes (e.g., temporal changes and land surface deformation) and anthropic activities result in temporal decorrelation.

- b) γ_{geo} : geometric decorrelation, which is also called baseline decorrelation, appears when incidence angles between the two acquisitions are different.
- c) γ_{DC} : doppler centroid decorrelation is induced by changes in viewing geometry in azimuth.
- d) γ_{vol} : volume decorrelation results from the volume of scatters, e.g., forest canopy, where the transmitted radiation scatters multiple times.
- e) γ_{noise} : thermal noise is affected by characteristics of sensors.
- f) γ_{pro} : different algorithms for data processing, e.g., master-slave co-registration and slave interpolation generate processing decorrelation.

2.1.2.2. Phase components

The phase difference ($\Delta\varphi$) between two image pairs in an interferogram involves different components. A general equation of these components concerning the total phase difference is shown below (Crosetto et al. 2016):

$$\Delta\varphi = \varphi_{disp} + \varphi_{topo} + \varphi_{atm} + \varphi_{orb} + \varphi_{noise} + 2k\pi \quad Eq.4$$

where φ_{disp} is the consequence of the ground deformation; φ_{topo} represents a residual phase due to the irregular shape of the Earth and topography; φ_{atm} is the result of the changes in the signal travel time because of the atmosphere or ionosphere between two acquisitions; φ_{orb} is caused by orbit errors; φ_{noise} is generated due to different scattering properties of objects on the ground. $2k\pi$ refers to wrapped phase modulo 2π , where k (integer number) is the multiple of 2π .

The known phase components that can be measured or neglected, pertinent to Equation 4, have to be subtracted to isolate the interferometric phase of ground displacements to generate deformation rates. The most considerable contribution is the component resulted from Earth's curvature and terrain elevation. The component can be simulated from a digital elevation model (DEM), then be removed from the displacement phase. The atmosphere effects may be removed by investigating long time series. Precise orbit information and filtering approaches may reduce orbit errors and noise errors, respectively.

2.1.2.3. Phase unwrapping

We can only extract the absolute phase modulo 2π from SAR acquisitions due to the limitation of signal transmitting and receiving models of the SAR system. The

continuous phase values are then wrapped into a cycle of 2π , causing phase ambiguity. Phase unwrapping is a process of reconstructing the absolute phase from the modulo 2π phase (Goldstein et al. 1988; Bamler and Hartl 1998).

2.1.3. Small Baseline Subset (SBAS) technique

A single interferogram can be generated along the LOS direction, from two acquisitions, based on the Differential Interferometry (DInSAR) (Rosen et al. 2000). The conventional method, however, is largely affected by the atmospheric phase component. To mitigate the atmospheric effects and generate deformation with multiple SAR images from different times, the SBAS algorithm developed by Berardino et al. (2002), was applied. The technique measures time series ground deformation using a set of chronologically ordered SAR images to mitigate setbacks of the interferometric decorrelation and the atmospheric phase error. The main steps, according to Berardino et al. (2002), are described below:

- i) Supposing that we have a set of $N+1$ SLC SAR images, over the same area, accessed in chronological order (t_0, \dots, t_N). M possible differential interferograms were generated with specifying threshold values of perpendicular baseline and temporal baseline, after co-registering images to the same reference grid in range and azimuth and removing flat-Earth component and topographic phase.
- ii) We assume that j interferogram was generated from two SAR images that were acquired at times t_B and t_A . The interferometric phase after unwrapping, in the pixel of azimuth and range coordinates (x, r) , can be expressed as the following equation:

$$\delta\phi(x, r) = \phi(t_B, x, r) - \phi(t_A, x, r) \quad \text{Eq. 5.1}$$

$$\approx \frac{4\pi}{\lambda} [d(t_B, x, r) - d(t_A, x, r)] + \phi_{topo,j}(x, r) + \phi_{atm,j}(x, r) + \phi_{noise,j}(x, r), \text{Eq. 5.2}$$

where $\phi(t_B, x, r)$ and $\phi(t_A, x, r)$ refer to the phase of the two images, which were accessed at time t_A and t_B , respectively. λ is the transmitted wavelength; $d(t_B, x, r)$ and $d(t_A, x, r)$ represent cumulative deformations at the LOS direction between times t_B and t_A regarding the first scene t_0 , assumed as a reference. $\phi_{topo,j}(x, r)$ is the topographic phase. $\phi_{atm,j}(x, r)$ corresponds to the phase component due to atmospheric effects. $\phi_{noise,j}(x, r)$ refers to the random noise phase.

- iii) The matrix form of a system of M equations in N unknowns can be denoted based on Equation 6, after removing phase contributions of topographic, atmospheric, and noise, as follows:

$$A\phi = \delta\phi, \quad \text{Eq. 6}$$

where A refers to an $M \times N$ matrix with respect to the set of interferograms and SAR scenes.

- iv) The unknowns can be replaced with the average phase velocity between time-adjacent acquisitions by manipulating the system in Equation 6. Then, the velocity can be expressed as follows:

$$v^T = [v_1 = \frac{\phi_1}{t_1 - t_0}, \dots, v_N = \frac{\phi_N - \phi_{N-1}}{t_N - t_{N-1}}] \quad \text{Eq. 7}$$

Then, we get the new equation by organizing Equation 7 in a matrix presentation, as follows:

$$Bv = \delta\phi, \quad \text{Eq. 8}$$

where B refers to an $M \times N$ matrix related to the unknown vector.

The minimum norm solution of the vector is generated by either the least-squares (LS) method or the singular value decomposition (SVD). The deformation time series can be derived based on the time intervals of SAR scenes. Lastly, atmospheric correction is applied to mitigate the atmospheric effect for the deformation time series.

2.2 Potential proxies for land subsidence

Land subsidence occurs when the pore pressure of aquifer sediments is reduced due to the large volumes of groundwater extraction. A decrease in pore pressure increases the effective stress, causing sediment compaction. The compressibility of the layer differs depending on the sediment properties of a layer and types of deformation. Sediments, i.e., clay, with low permeability of the layer compact much more than materials, i.e., sands, with high permeability. The compaction of sediments with different properties is either elastic or inelastic. When groundwater head drops below the consolidation head, sediments deform inelastically, which results in irreversible (permanent) subsidence (Smith et al. 2017). This only occurs in the unconsolidated fine-grained

materials such as clay. Elastic deformation occurs when the groundwater head is above the previous lowest level. In this case, the deformation is reversible when the groundwater head recovers (both clay and sand). The total deformation that is proportional to the head changes (Δh) can be described with skeletal specific storage coefficient (S_{sk}), which represents the compressibility of aquifer layers, and b_0 , which reflects the changes in sediment thickness, as follows:

$$\Delta b = S_{sk} \times \Delta h \times b_0 \quad Eq. 9$$

The above-mentioned parameters are challenging to estimate in the area where lacks in-site monitoring. However, an alternative method using satellite-based data and deep learning algorithms can be used to overcome groundwater data scarcity issues for the proxies for groundwater dynamics, considering the groundwater is the main source for irrigation should be used. These include a) actual evapotranspiration(ETa), which potentially estimates crop water use and thus reflects groundwater demand in this area; b) land surface temperature(LST) that may affect evapotranspiration rate and subsequently the dynamics of groundwater consumption; c) the normalized difference vegetation index (NDVI), which indicates the greenness of vegetation cover and reflects the vegetation growth as a function of groundwater usage; d) precipitation(P) that recharges the aquifer; and e) soil water index(SWI), which represents soil moisture. This study integrates the five above-mentioned proxies together with the InSAR deformation measurement using a deep learning algorithm to estimate historical and near future land deformation due to agricultural groundwater pumping over the test area.

2.3 Study area

The Shabestar basin is located in the East Azerbaijan Province in northwestern Iran (Figure 3). The basin covers an approximate area of 500 km², delimited on the north by the Mishow Mountain, on the west by the Tasuj Plain, on the southeast by Tabriz City, and on the southwest by Urmia Lake. The Shabestar Basin is a part of the Lake Urmia Basin, with the highest and lowest altitude of 1850 and 1275 m above mean sea level, respectively. The altitude decreases from north and northeast towards the south, with an average slope of 3%. The climate of the area is semi-arid with the mean annual temperature of 11.5 °C, and the average annual precipitation of approximately

350 mm. The dry season occurs between June and October; the wet season lasts from the end of October to May. In the study area, all rivers including Derechay, Heriz, Mashnagh, Sufiyan, and Tilchay have intermittent flow regimes, except river Daryanchay, which exhibits a permanent flow. These rivers, which originate from the south aspect of Mishow Mountain and flow toward the southwest, have created fertile soils for agriculture. Because of deficiency in surface-water sources except for seasonal rivers. As agriculture is highly dependent on groundwater reserves, the groundwater table declined by 4.9 m per year on average, recorded from 2004 to 2014 by East Azerbaijan Regional Water Authority (EARWA). The water table drops to the lowest level near the end of the irrigation season in October and reaches the highest in June. According to the report by EARWA (2015), the greatest groundwater pumping was found in the southeast in the vicinity of Nazarlu.

2.3.1 Geological and hydrogeological setting

The Kahar formation, as the oldest formation in the study area, underlies in the northernmost region (Figure 3). The lithological formation is composed of micaceous sandstone, shales, sericite, and schists, of the Precambrian age. The thickness of the formation in the region is around 1400 m. Furthermore, the Barut formation with a thickness of about 800 m comprises alternations of chert crystalline dolomite and micaceous shale of the region pre-Cambrian age. Marly limestone and igneous rocks of the Permian age outcrop in the north part of the study area. Also, massive, recrystallized grey to white limestone and flysch-type deposits crop out in the northern part of the basin during the late cretaceous age. The main fault zone of the study area expands from northeast towards west close to Lake Urmia, separated the Neogene and Quaternary unit in the northern part of the study area. Conglomerates and red sandstone of the late Miocene, found in the west and central part of the study area, are composed of dark dolomites and sandstone. Quaternary terrace-alluvium distributed in the central area forming the old alluvial deposits, which include conglomerates with a matrix of clay and silts; young alluvial deposits, which consists of terrace deposits close to seasonal rivers; salt deposits with clay near Lake Urmia; sandy deposits; and river gravel. Various formation in the study area forms fertile soil for agricultural activities but is susceptible to compaction and results in land subsidence.

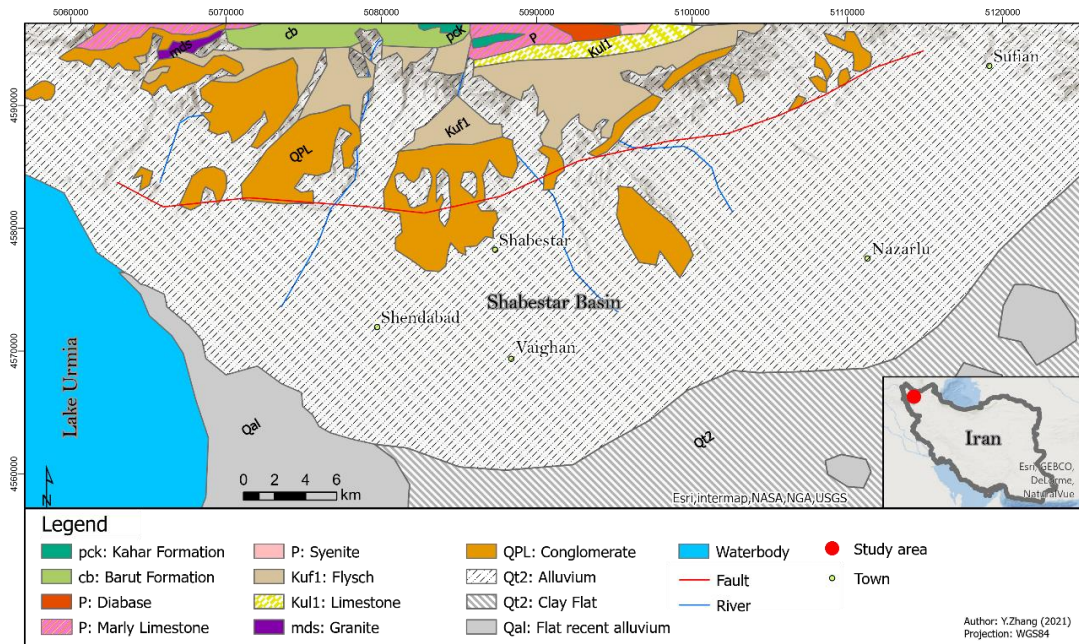


Figure 3. The geological map of the study area. Reproduced Eftekharnjad et al. (2000) and Mehr et al. (2019). Background maps © Esri

The Shebestar aquifer extends from the north highland to the middle of the basin. The thickness of the aquifer with the alluvial deposits mainly containing silt and clay, in close proximity to the city Nazarlu, reaches the greatest about 300 m. According to historical geophysical surveys and drilling records, the aquifer thickness gradually decreases towards the area with Neogene unit in the vicinity of the highland areas. Based on previous pumping tests by EARWA (1997), high transmissivity, which varies from 1000 to 1500 m² per day, is noted in the middle of the studied aquifer. The transmissivity gradually reduces with the changes in aquifer thickness. Area with low transmissivity (43 m² per day) is observed in the vicinity of the mountain.

2.3.2 Related study

A very few studies have been conducting the InSAR technique to estimate subsidence and assist groundwater management in the study area. Nadiri et al. (2018) evaluated the subsidence vulnerability in the Shabestar Basin using a new framework, ALPRIFT. The model considered seven variables that may affect subsidence, including aquifer media, land use types, groundwater pumpage and recharge, the impact of aquifer thickness, fault distance, and groundwater level from 2015 to 2016. The study obtained InSAR ready products with a resolution of 10 m in 2015-2016 from the

European Space Agency (ESA). They adjusted the InSAR data using 10-year ground-truth data at observation wells for modeling. Their research reveals subsidence rates ranged between -100 and -50 mm in the westernmost of the basin, and subsidence rates ranged from -50 to -25 mm in the eastern part during the 2015-2016 period. According to their findings, the area in the eastern part of the basin was more vulnerable to subsidence than the area in the center and western part of the basin. The subsidence vulnerability was moderate in most of the areas in the west, except the place in the westernmost of the study area. The easternmost part of the basin was estimated to have a high risk of being affected by subsidence.

3. Data and Methodology

3.1 SBAS InSAR-derived deformation

In this section, we illustrate the data to estimate mean deformation rates and time-series displacements; furthermore, we introduce approaches to derive annual mean deformation velocities at the line-of-sight (LOS) direction and deformation time-series. We subsequently decomposed LOS deformations into vertical components. Lastly, the difference between deformation rates from both tracks was determined for validation purposes.

3.1.1. Data used

The Sentinel-1 mission consists of two satellites, Sentinel-1A and Sentinel-1B, which are launched by the European Space Agency (ESA) through Europe's Copernicus program. Sentinel-1A and -1B were launched in April 2015 and April 2016, respectively. A single satellite is designed to carry a C-band synthetic-aperture radar instrument providing polar-orbiting, 24-hour, and all-weather imagery with a resolution of down to 5 meters and covering up to 400 kilometers (Torres et al. 2012). The satellite in a single pass(ascending or descending) provides SAR imagery with a 12-day revisit period. Sentinel-1 with The Interferometric Wide (IW) swath mode implementing Terrain Observation with Progressive Scans SAR (TOPSAR) supports dual-polarization (HH+HV and VV+VH) and provides SAR imagery with three

sub-swaths (IW1, IW2, and IW3) in a single look pattern with a wide coverage up to 250 km and high resolution of 5 m by 20 m (De Zan and Guarnieri 2006).

In this research, we obtained 128 ascending data and 125 descending Sentinel-1A TOPSAR data with vertical polarization, covering the Shabestar Basin, from Copernicus open access hub (<https://scihub.copernicus.eu/>) to estimate long-term land surface deformation velocity and deformation time series. Properties of the data are indicated in Table 1. Two datasets had an overlapping time span from 22 January 2016 to 21 October 2020. The three-arc second Shuttle Radar Topography Mission (SRTM) DEM, which is available through the National Aeronautics and Space Administration (NASA), was acquired to eliminate topographic phases. Precise orbit determination (POD) provided by the ESA was adopted for orbit refinement and phase re-flattening.

Table 1. Description of Sentinel-1A images from both tracks.

	Ascending	Descending
Production types	Sentinel-1 level-1 SLC IW	
Polarization	Vertical-Vertical (VV)	
Number of scenes	128	125
Relative Orbit number	174	79
Azimuth angle (degree)	-100.3	100.2
Mean Incidence angle of the study area (degree)	38.7	37.1

3.1.2 Data processing

We estimated annual mean surface subsidence velocity and long-term deformation time-series along the LOS and vertical direction in the Shabestar Basin using the SBAS-InSAR technique. The data was processed by an open-source InSAR processing software GMTSAR (Sandwell et al. 2011a; 2011b). The SBAS analysis was performed with ascending and descending data separately in GMTSAR to check the accuracy of our analysis using two independent SAR data sets. The main steps are illustrated in the following sections.

3.1.2.1. Interferograms Stacking

The sentinel-1A IW1 and IW2 from the ascending orbit and IW2 from the descending pass covering the study area were selected. Images on 16 July 2018 from ascending orbit and on 10 July 2018 from descending pass were chosen as master images for the two groups of datasets, respectively (Figure 4a and 4b). Co-registration was performed to obtain interferometric phase coherence. The slave images were aligned with the master image using the Precise Orbital Information (POD) to evaluate sub-pixel accuracy in the range and azimuth before forming interferograms. A Golden section search algorithm (Press et al. 1992) in GMTSAR was applied to estimate the range and azimuth shift based on the orbit information, and then the 2-dimensional (2D) cross-correlation algorithm with a search window size of 64 pixels was used on small patches to perform an accurate image co-registration (Sandwell et al. 2011a). After completing the image alignment, mountainous areas and water bodies were extracted from each image to avoid extended distortions and noises on inferring image pairs. The differential interferograms were generated based on the perpendicular baseline shorter than 150 meters. A small temporal baseline, 90 days, was selected as the second criterion to form interferograms since the study area was mainly agricultural fields affected by the temporal decorrelation. Finally, 764 ascending and 779 descending differential interferograms were generated.

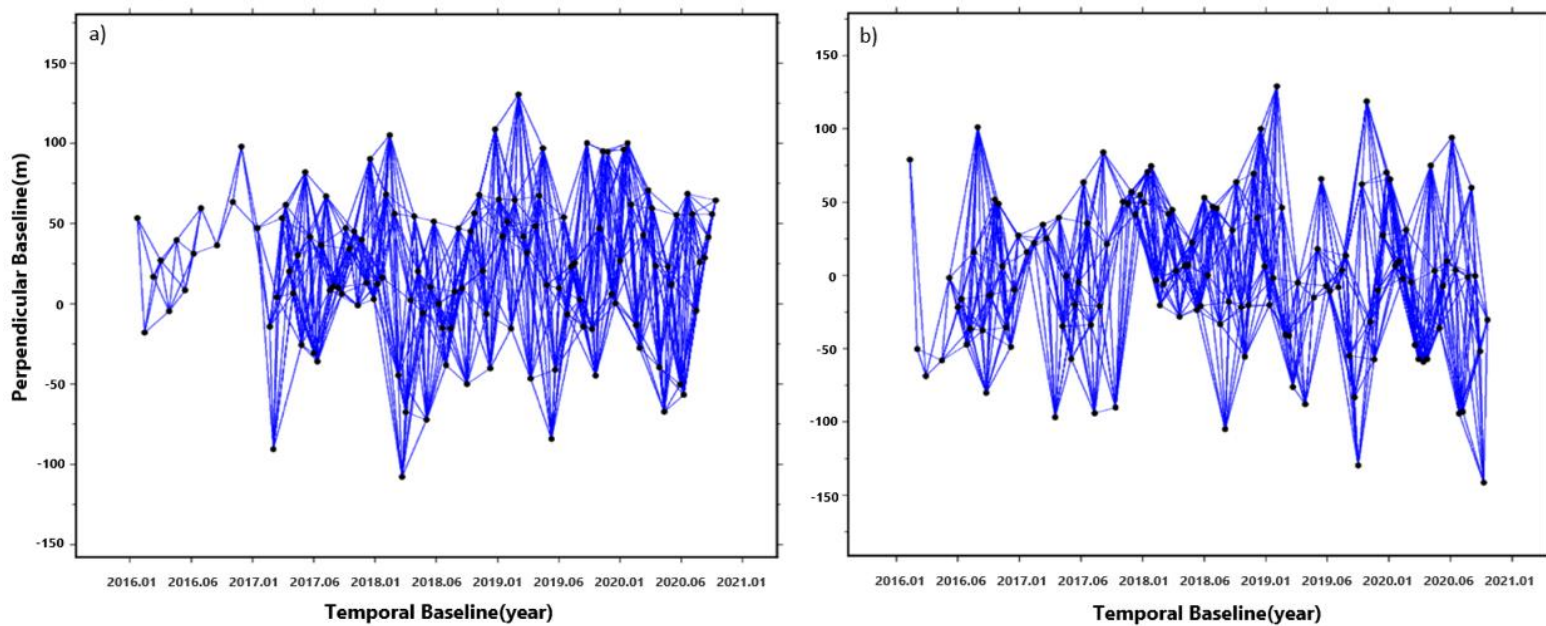


Figure 4. Temporal and perpendicular baselines of Sentinel-1A images interferometric pairs from ascending (4a) and descending (4b) tracks. Blue lines indicate interferometric pairs.

After co-registering images and generating interferograms, the orbit information was used to eliminate the flat-Earth phase component because of the Earth's curvature. Next, the topographic phase parameter was removed using the three arc-second SRTM DEM. Furthermore, interferogram noise was eliminated using a Goldstein adaptive filter (Goldstein and Werner 1997; Baran et al. 2003). Coherence values that were less than 0.075 on the interferograms were discarded to remove unreliable phase values for further analysis. Phase values on a set of filtered interferograms were unwrapped using a 2D unwrapping tool, SNAPHU (Chen and Zebker 2002), which was provided in GMTSAR. We estimated mean LOS displacements and deformation time-series for ascending and descending data using the SBAS algorithm independently. Mean incidence angles from both tracks were calculated by extracting the incidence angle of each pixel on the set of interferograms for the SBAS analysis. Lastly, the atmospheric correction was performed to reduce atmospheric effects in the InSAR measurement.

3.1.2.2. LOS Deformation Decomposition

SBAS-InSAR-derived displacements only provided the 1-dimensional deformation in the direction of line-of-sight (LOS) in milometer. Deformation rates that were generated from two orbits, ascending and descending, have two different viewing geometries. Therefore, it is possible to retrieve two of the three-dimensional velocity components (V_N , V_E , and V_h). Because Sentinel-1 is a polar-orbiting, LOS measurements are insensitive to the deformations in the direction of north-south (Wright et al. 2004). In addition, we assume there was no horizontal movement because SAR is sensitive to the vertical direction. Annual mean SBAS-InSAR LOS rates from both orbits were then decomposed into vertical components (V_v) with neglecting the north-south (V_N) and the horizontal movement (V_h). LOS measurements were geocoded and resampled to the same spatial resolution, 85×85 m within the same frame, using the nearest neighbor method to minimize the effects of spatial mismatching. Each pixel of the LOS rate from both orbits was then decomposed into vertical components according to Equation 10 (Motagh et al. 2017).

$$V_v = \frac{V_{los}}{\cos\theta}, \quad Eq. 10$$

where θ represents the incidence angles of the study area.

3.1.2.3. Inter-comparison

Since there was no permanent GPS station in the area, we processed both ascending and descending data to validate our InSAR analysis. Mean deformation rates obtained from ascending data were compared with rates from descending data, pixel by pixel, for validation. Both images were resampled into an 85×85 m regular grid within a common reframe. The root-mean-square error (RMSE) was applied to estimate the difference between pixel values on both images as well, a Pearson correlation coefficient was used to investigate the consistency between these two spatial patterns.

3.2 Hydrological variables and deep learning method

In this section, we introduce the satellite products of hydrological variables (section 3.2.1), including the actual Evapotranspiration (ETa), Land surface temperature (LST), nominalize difference vegetation index (NDVI), precipitation (P), and soil water index (SWI), associated with InSAR-derived subsidence. We subsequently harmonized all satellite data to the spatial resolution of the displacement data (85×85 m) for further analysis (section 3.2.2). The study area was divided into five zones, where mean vertical velocities ranged from above -90, -90 to -70; -70 to -50; -50 to -30; and -30 to -15 mm/year according to the measured average InSAR-derived subsidence velocities in section 4.1 for spatial and temporal analysis. Considering the different time lag between each variable and the measured subsidence by InSAR technique, we calculated lag correlation coefficients with the maximum time interval of 300 days over the whole period (Section 3.2.3). The multivariate deep learning model, Long short-term memory (LSTM), was then used to derive the importance of variables and predict future displacements (section 3.2.4).

3.2.1. Data used

Remote sensing-based products of ETa, LST, and NDVI with a high spatial resolution of 30 m were acquired from the Earth Engine Evapotranspiration Flux (EEFlux) (Allen et al. 2015). Due to the unavailability and quality of ground-truth data in the region, daily satellite precipitation and SWI products at fine resolutions were downloaded from the Center for Hydrometeorology and Remote Sensing (CHRS) and Copernicus Global Land Service (CGLS), respectively. Information about

satellite-based products is described in Table 2. Algorithms for generating the actual ET, LST, NDVI, P, and SWI are described in the following sub-sections (3.2.1.1-3.2.1.5).

EEFlux application operates on the Google Earth Engine platform (GEE) and provides Landsat-based ready products with a high spatial resolution of 30 m. Taking the benefit of GEE, which provides a full archive of the Landsat image collection, EEFlux uses Landsat-7 and Landsat-8 images to derive daily ET within a users-defined reframe based on the METRIC algorithm (Allen et al. 2007b). The accuracy of ETa estimations provided by EEFlux has been examined in Argentina (de Oliveira Costa et al. 2020), Brazil (Salgado and Mateos, 2021), and Guatemala (Mayes et al. 2020), suggesting that EEFlux gives accurate information about ETa. The engine can also generate other Landsat-based products, such as albedo, LST, NDVI, and reference evapotranspiration from 1984 to the present.

In this study, we obtained 155 ready-products of ETa, LST, and NDVI within two frames covering the whole study area from 2016 to 2020. These satellite products were derived from Landsat 7 (Path/Row 168/34 and 169/33) and Landsat 8 (Path/Row 168/34 and 169/34). Images selected in the dry season were all cloud-free or had cloud rates less than 2%, while images selected in the wet season had cloud rates less than 10%. Cloud contaminations in images were filled with a robust method, ordinary kriging (Zhang et al. 2007; Pringle et al. 2009), using the MATLAB software.

We acquired a set of daily satellite precipitation products and SWI products covering the period of five years with 1756 days in total. The precipitation products based on the PERSIANN-Cloud Classification System (PERSIANN-CCS) (Hong et al. 2004) were found to have the highest spatial resolution, 4 km, covering the study area. The accuracy of PERSIANN-CCS in Iran has been examined in several studies such as Moazami et al. (2014) and Mosaffa et al. (2020), which demonstrate the dependability of PERSIANN-CCS to estimate real-time satellite precipitation. SWI images with a resolution of $0.01 \times 0.01^\circ$ characterize soil moisture conditions at different depths based on measurements of surface soil moisture from Sentinel-1C SAR and the Advanced SCATterometer (ASCAT) (Bauer-Marschallinger et al. 2018). The SWI that characterizes soil moisture condition was evaluated in several papers, such as Brocca et al. (2010) and Paulik et al. (2014), which revealed positive results.

Table 2. Description of satellite-based hydrological variables.

Date product	Spatial resolution	Temporal resolution	Unit	Data sources
ETa	30m	Min-Max: 1-48 days	mm	https://eeflux-level1.appspot.com/
LST	30m	Same as above	Kelvin	Same as above
NDVI	30m	Same as above	/	Same as above
P	4km	Daily	mm	https://chrs.web.uci.edu/
SWI at T=2	1km	Daily	percent	https://land.copernicus.eu/

*Note: T means T-value, which represents different depths of soils.

3.2.1.1 METRIC algorithm and actual ET

EEFlux calculates the energy balance of land surface and albedo with the thermal and reflection imagery of Landsat. The surface energy balance of each scene is calibrated using hourly North American Land Data Assimilation System gridded weather data. The ETa is measured as a residual of the surface energy balance (Allen et al. 2007a; 2007b). The algorithm, according to Allen et al. (2007a; 2007b), is summarized below:

Firstly, the latent heat flux (λE) is calculated at the exact satellite overpass time to derive the actual evapotranspiration (ET_a) for each pixel. The expression is as follows:

$$\lambda E = Rn - G - H, \quad Eq. 11$$

where Rn is net radiation ($W m^{-2}$); G represents soil heat flux in ($W m^{-2}$); and H denotes sensible heat flux ($W m^{-2}$).

Secondly, the instant ET (ET_{inst} in $mm h^{-1}$) is derived from the latent heat flux (LE) by dividing the latent heat of vaporization as follows:

$$ET_{inst} = 3600 \times \frac{LE}{\lambda \times \rho_w}, \quad Eq. 12$$

where λ is the latent heat of vaporization (Jkg^{-1}); ρ_w denotes water density (kgm^{-3}).

Thirdly, the fraction of reference evapotranspiration (ET_o) expressed as ET_rF is computed by the ratio of the derived instant ET to the reference evapotranspiration (ET_r):

$$ET_{rF} = \frac{ET_{inst}}{ET_r} \quad Eq. 13$$

Lastly, the daily ET_a for each pixel on the image can be calculated by multiplying daily ET_r , assuming ET_{rF} at the satellite overpass time is accorded with the daily ET_r . The expression is shown as follows:

$$ET_a = ET_{rF} \times ET_r \quad Eq. 14$$

3.2.1.2 Normalized Difference Vegetation Index (NDVI)

NDVI is one of the most widely used vegetation indices that can quantify vegetation greenness. NDVI is a ratio between visible red(R) and near-infrared (NIR) light from vegetations. The expression is shown as follows:

$$NDVI = \frac{(NIR - Red)}{(NIR + Red)} \quad Eq. 15$$

Most of the red light is absorbed by the chlorophyll pigment in a healthy plant, and most of the NIR light is reflected by the cell structure. It means areas covered by dense vegetation will reflect fewer R light and more NIR light. NDVI values range from -1 to 1. Negative values (close to -1) of NDVI denote water; Values approaching zero indicate bare lands; positive values (approximately 0.2 to 0.4) of NDVI correspond to shrub and grasslands; Values close to 1 represent dense vegetation cover.

3.2.1.3 Land surface temperature (LST)

Land surface temperature (LST) measures the ground surface temperature in Kelvin. LST products in EEFlux are generated from Landsat images utilizing a fixed atmospheric calibration proposed by Allen et al. (2007b).

3.2.1.4 Precipitation(P)

The PERSIANN uses Artificial Neural Networks (ANN) to estimate the precipitation rate for each pixel from the geosynchronous satellite longwave infrared imagery every 30 minutes (Sorooshian et al. 2000). PERSIANN-CCS is a cloud-patch based algorithm, which extracts features from the cloud coverage using different incremental temperature thresholds. The algorithm, compared to PERSIANN, utilizes more information from the infrared cloud images by segmenting the cloud images into patches with an incremental temperature threshold. The main steps of the algorithm,

according to Hong et al. (2004), include segmenting cloud images into patches; extracting features including dynamic evolutions, cloud top heights, geometry properties, and textures from the patches for the identification of cloud types; categorizing these features using the clustering algorithm; and constructing a relationship between the brightness temperature of cloud patches and the precipitation rate using probability matching method and nonlinear exponential curve fitting. The rainfall estimation is calibrated using passive microwave satellite (PWM) rainfall data. The PERSIANN-CCS and algorithm are discussed in detail in Hong et al. (2004) and Karbalaee et al. (2017).

3.2.1.5. Soil water index (SWI)

The retrieval algorithm of SWI is based on a two-layer balance model developed by Wagner et al. (1999). The algorithm sums up and exponentially weighs past measurements of surface soil moisture based on a characteristic time length (T). T values initially represent the effects of the past measurements on current measurements of SWI. Conceptually, soil moisture in the surface layer is temporally highly dynamic because it directly contacts with the atmosphere. The dynamic is decreased with an increase of soil depth since the volume of water stored in a reservoir soil layer depends on the infiltration of water filled in the surface layer. As previous soil moisture conditions control the amount of water stored in the reservoir layer, the T value for the SWI calculation is a ratio of the depth of the reservoir layer to a pseudo-diffusivity constant. A higher T value denotes a deep soil layer if the soil diffusivity is constant. The original SWI values were required to convert to meaningful physical values ranging from 0 to 100% based on a given a scale factor.

3.2.2. Data interpolation and harmonization

To reduce the effects of spatial mismatching for further analysis, all satellite-based products of hydrological variables from different sources with different spatial and temporal resolutions were transformed to the spatial resolution of InSAR-derived deformation date set and interpolated into daily scale.

The data interpolation and harmonization method for ETa, LST, and NDVI satellite products was done using a similar approach because these images from EEFlux were at the same spatial and temporal resolution. The satellite images from two frames on

the same date were firstly merged in ArcGIS pro. These images were subsequently interpolated into daily data using 3D linear interpolation (2D images + time) methods with the 20-day moving average technique in MATLAB. The interpolation method is explained below using ETa products as an example.

ETa images were organized in a 2D spatial array. Each image provided the ETa values, E , in the array at a time t . A time-series (t_i, E_i) , $i=1, 2, 3, \dots, N$ was gathered at a location (m, n) by extracting the values at the location consecutively in the array (Figure 5). This set of values at each position on the image were subsequently used to fill the gaps in time series using linear interpolation with a 20-day moving average. Linear interpolation is one of the most used interpolation methods, which assumes the predicted points (E) lie on the line joining the neighboring points from left (E_i) and right (E_{i+1}). If we assume E -data points at a position (m,n) are in ascending order, then we have $E_i < E_{i+1}$ and $E_i < E < E_{i+1}$. The E -point at the time-series using the linear interpolation can be expressed as follow:

$$y(E) = y_i + \frac{(y_{i+1} - y_i)(E - E_i)}{(E_{i+1} - E_i)} \quad Eq. 16$$

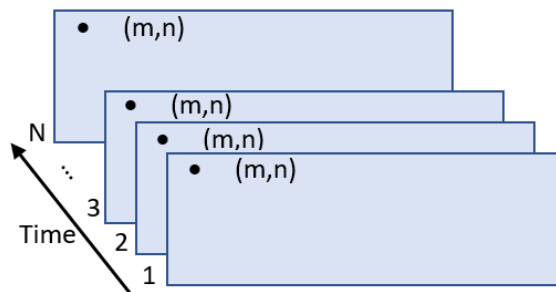


Figure 5. Concept diagram of a 3D array for image interpolation. © Yixin Zhang (2021)

Daily ETa, LST, and NDVI, with a spatial resolution of 30×30 m over 1756 days, were subsequently aggregated to the spatial resolution of InSAR-derived displacements, 85×85 m, in ArcGIS pro.

Downscaling approaches have two categories, which are statistical and dynamical methods. Statistical downscaling techniques enhance a low-resolution image to a fine resolution using additional high-resolution data such as NDVI, elevation, and temperature (Immerzeel et al. 2009; Fang et al. 2013). Nevertheless, the deep learning approach in this study requires variables to be independent. Dynamic downscaling

methods adopt a regional climate model (RCMs) or numerical weather model (NWMs) to enhance image resolution, but the technique requires enormous computational resources. Therefore, to obtain an 85 m resolution daily precipitation and SWI data, a simple downscale strategy was performed using a near-neighboring method in ArcGIS pro.

InSAR-derived vertical deformation time series from ascending and descending tracks were resampled into the previously mentioned spatial resolution (85×85 m) in section 3.1.2.2 using a near-neighboring approach and clipped to the area of interest in ArcGIS pro environment. The set of images from both orbits were combined and interpolated into daily data using the linear interpolation method with the 20-day moving average.

Before determining the time lag for each variable and fitting models in different zones, it is required to detrend the InSAR-derived deformation time series. This is because correlation analysis and the deep learning method, LSTM, assume each pair of observations is independently distributed. However, the deformation values at time t were derived from its value at $t-1$, which did not comply with the assumption. Consequently, it is necessary to detrend the time series in order to conform to the assumption. In the study, the least-squares fit (a linear trend) of the time series values was removed from the data.

3.2.3. Time lag

Different characteristics of sediments result in the time lag between the driving factors and land subsidence displacements. Time lag can influence the correlation between dependent and independent variables and thus result in inaccurate prediction by a model. Therefore it is essential to identify the delay between different variables and subsidence.

Daily average values of each variable were initially extracted for five subsidence zones at each date. We subsequently performed a cross-correlation analysis using Python scripting language to evaluate the time lag between mean values of ETa, LST, NDVI, P, and SWI and the detrended InSAR deformation time series in the five subsiding zones from 2016 to 2020. Cross-correlation is a measure of similarity between two time series. Cross-correlation coefficient (R) between a time series (Y_1)

and the dependent time series (Y_2) at time lag τ can be expressed as follows:

$$R(\tau) = \frac{Cov'(Y_1, Y_2)}{S'_{y1} \times S'_{y2}} \quad Eq. 17$$

where Cov' is the covariance of overlapped segments of two time series; S'_{y1} , S'_{y2} denote the standard deviation of overlapped segments of the two time series; $R(\tau)$ represents cross-relation coefficient at time lag τ . The lag coefficient ranges between -1 to 1. A cross-correlation coefficient below zero and above zero indicates a negative and positive correlation between two cumulative datasets. Values close to 1 or -1 indicate a high direct or inverse correlation between the two variables, respectively.

In this study, the lag correlation coefficient was calculated to analyze the lag time of deformation response to changes in five hydrological variables. Since land sinking is displayed with negative numbers, deformation values were multiplied by -1 in order to intuitively present subsidence with positive numbers. The maximum negative or positive correlation coefficient and its corresponding time lag were extracted for each variable. The expression of the approach is described as follows:

$$R = \max\{R_0, R_1, R_2, R_3 \dots, R_n\}, \quad Eq. 18$$

where R is the lag correlation coefficient between $R_0, R_1, R_2, R_3 \dots, R_n$, which are the ETa, LST, NDVI, P, or SWI, and the subsidence time series from 0 to n days. For instance, If $R=R_n$, the lag time of deformation response to hydrological variable changes is n days.

In this study, we considered the maximum lag time of 300 days over the period of time deemed to be sufficient according to the literature. This means the times associated with the deformation were incremented by 1, 2, 3, ..., 300 days. The maximum lag correlation coefficient within the time frame of 300 days was extracted, and its corresponding time lag was considered as the lag time, which was used to amend time shifts between hydrological variables and deformation changes for further modeling.

3.2.4. Multivariate Long short-term memory (LSTM) modeling

A time-series multivariate deep learning model, LSTM, was used to derive the importance of the hydrological variables in subsidence occurrence and predict near future displacements for each zone. It has been shown that the performance of a time-series LSTM model in a predicting task is superior to that of ARIMA, Support Vector Machine, and Random Forest (Zhang and Nawata 2017; Siami-Namini et al. 2018).

LSTM (Hochreiter and Schmidhuber 1997) is an extension of recurrent neural network (RNN), which can conduct long-distance dependence that RNNs cannot learn by a forgetting mechanism. LSTMs, like all RNNs, have a chain structure involving repeating modules of neural networks. Unlike other RNNs with a single neural network in the repeating module, LSTMs have four neural network layers, which have a special way to interact. In the repeating module, the LSTMs memory cells involve a memory cell (c_t) and a working cell (h_t), which save the information controlled by the gates. Cell states in the LSTM consist of two activation functions: sigmoid and tanh. The forgetting gate firstly reads the formal cell state (h_{t-1}) and the current input (x_t), and decides information that will be forgotten. The selected information is then stored in the memory cell(c_t). The input gate (i_t) subsequently chooses new information that will be saved in the memory cell. The output gate (o_t) consequently controls the part of the memory cell to be remembered and outputs the information in the memory cell to the working cell (h_t). The LSTM cells are illustrated in Figure 6.

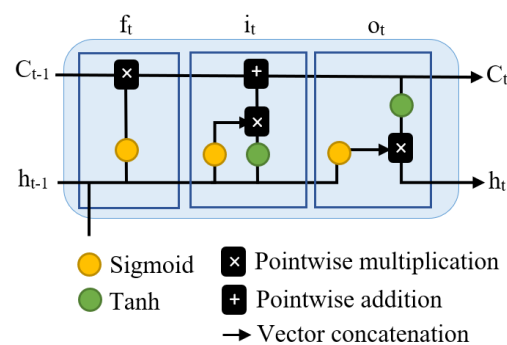


Figure 6. Concept diagram of the LSTM cells.

© Yixin Zhang (2021)

An LSTM model for each zone was constructed using Keras with Tensorflow 1.14.0 in the Python environment. The concept of the LSTM model is described in Figure 7. Each model contains three hidden layers with a hidden unit of 96 each. A dropout,

omitting 30% of the nodes, was applied to avoid model overfitting. The model should be compiled and parsed in order to conform to the mathematical characters and conventions used in TensorFlow when the network is established. A loss function, mean squared error, with an optimization algorithm called 'Adam' was used when compiling the model.

The input dataset contains series of mean values of detrended InSAR-derived deformation and three hydrological variables: ETa, LST, and NDVI in five subsiding zones. We only selected three variables because of weak correlations between deformation time series and precipitation and SWI variables. The dataset was split into 60% training and 40% testing at 150-time-step. The valid days at the time steps of the training and testing data sets were 903 and 553. We initially examined the model with different parameters several times and selected a model with the best goodness of fit. The number of epochs, which represents the number of times the dataset is fitted to this model, was set to 150. To reduce overall memory used, the batch size, which is the number of samples utilized in one iteration for training, was considered 21. Because the objective is to train an optimized model with remembering the values from earlier stages, it is necessary to set the data shuffling option to false. Training a model with the same parameters was repeated three times to select a model with the best goodness of fit.

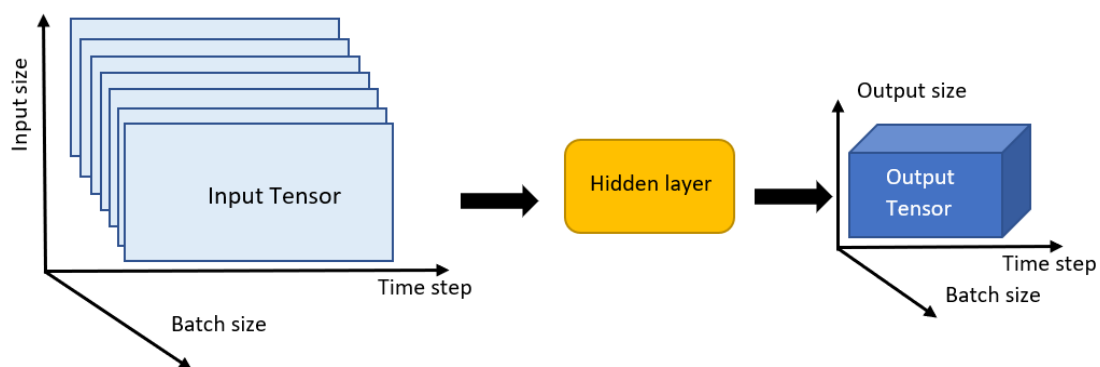


Figure 7. Concept diagram of an LSTM model. A tensor is a matrix of n -dimensions. Each sample in the tensor is represented in a 2D array with a size of $\text{time step} \times \text{input size}$. The input size corresponds to the number of features or variables. Time step represents the length of input series and the network memories. Batch size is the number of such 2D arrays utilized in one iteration for training. The input tensor was put in hidden layers. Each hidden layer involves multiple memory cells, where executes nonlinear transformation to inputs and directs them through activation functions as output (see Figure 6). The output size in a output tensor is the number of dependent variable. © Yixin Zhang (2021)

The mean squared error (MSE) and root mean squared error (RMSE) were used to represent the loss function and evaluate the performance of the built model, respectively. We used the trained model to forecast the test dataset and obtained RMSE values in five subsiding zones. After evaluating the performance of the model, deformation rates in the next five years after 21 October 2020 were predicted using the current and previous dataset with the built model for each zone. The linear trend information, which was removed during the analysis, was added back to the predicted data.

The determination of permutation importance in a deep learning model is usually in a 2D array. Since the input of LSTM layers in Keras took the form of a 3D array, the importance of variables in the model was estimated using the SHapley Additive exPlanations (SHAP) (Lundberg and Lee 2016) package in Python. The SHAP explanation approach performs Shapley values from coalitional game theory. Values of the features (or variables in this study) are players in the coalition. The explanation of SHAP is described as follow:

$$g(z') = \phi_0 + \sum_{j=1}^M \phi_j z'_j \quad Eq.19$$

where g is the explanation mode; $z' \in \{0,1\}^M$ represents coalition vector, a value of 1 denotes that the feature value is present, and 0 means the value is absent; M corresponds to the maximum size of the coalition; and $\phi_j \in \mathbb{R}$ means the feature attribution for the Shapley values of a feature j .

The Shapley values determine the importance of features or variables in the LSTM model. Variables with high absolute Shapley values are important. Since the objective is to obtain global importance, it is necessary to sum the absolute Shapley values per variable among the data. We subsequently used a SHAP summary plot to rank the feature importance. The range of Shapley in the plot is dependent on the range of output magnitude of the model.

4. Result

4.1 InSAR-derived deformation

Ascending and descending SAR data analysis was performed in the GMTSAR software, with 128 and 125 acquisitions, respectively. Annual average subsidence rates along the line-of-sight (LOS) direction using the SBAS-InSAR technique for both tracks over the period of 2016-2020 in the Shabestar Basin for both ascending and descending data are shown in Figure 8. LOS deformation maps from both tracks with the same spatial resolution of 85×85 m illustrated similar spatial patterns and magnitude that show the validity of our InSAR calculation. Negative values, which are dominated in the middle part of the study area, represent land subsidence. Mean deformation rates derived from the two datasets ranged from -77 to 10 mm/year.

The results from the two data sets illustrate a good agreement within the deforming area. The largest subsidence velocity of -77 mm/year at the center of the depression was observed near the town of Nazarlu. The rate gradually reduced in all directions. A slight difference was detected in the easternmost and the westernmost parts of the study area between the two tracks, where the subsidence rates derived from ascending data were slightly higher than those from descending data. Despite the slight difference, the two spatial maps detected the same area of the largest subsidence in the basin. Prominent subsidence was found in the eastern and western portions of the basin, where subsidence rates ranged from -70 to -15 mm/year. Areas that are located near Mishow Mountain were not affected by the subsidence between 2016 and 2020. The average vertical deformation patterns from the two datasets are discussed below.

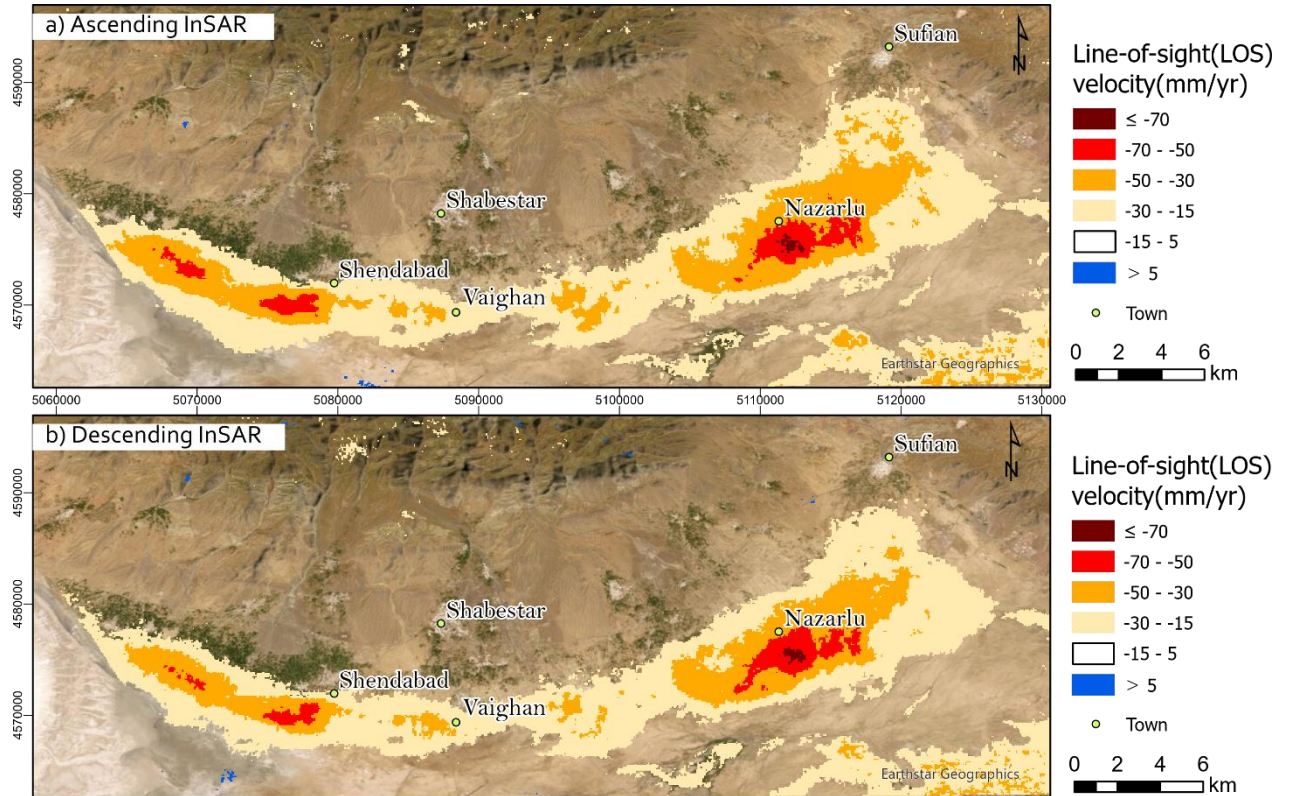


Figure 8. (a) Line-of-sight (LOS) velocity maps derived from Sentinel-1A ascending orbits; and (b) LOS velocity maps from Sentinel-1A descending track. Positive values colored in blue indicate uplift and negative values represent subsidence.

Because of a lack of GPS and leveling data, inter-comparison between LOS displacements from ascending and descending tracks were performed. Figure 9 illustrates the correlation between both ascending and descending data sets. We found that the RMSE value between the two images was 3.1 mm, and the correlation coefficient value (R-squared) was 0.91. These reveal that mean deformation rates from ascending and descending datasets are highly correlated. The difference of all common pixels within the deforming area follows the approximately normal distribution, as illustrated in Figure 9b. Very small numbers of pixels from the two datasets showed about 10 mm difference. Despite the difference, the inter-comparison between two images and the spatial distribution of subsidence from two datasets reveals similar vertical motions between 2016 and 2020, leading to reliable results.

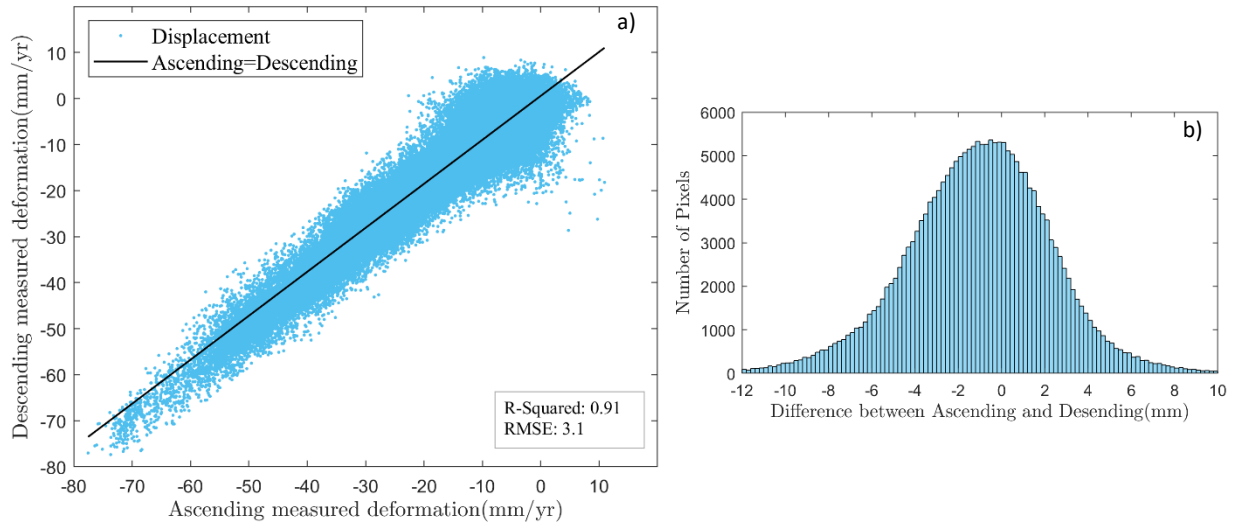


Figure 9. Comparison of mean LOS deformation velocity between ascending and descending orbits. a) Correlation between the LOS deformation rates from the two different datasets. b) Difference analysis between the ascending and descending tracks.

A comparison of the decomposed deformation velocities between ascending and descending InSAR measurement to illustrate vertical motions in the study area between 2016 and 2020 is shown in Figure 10. The annual average deformation was decomposed from the LOS direction to the vertical direction, pixel by pixel, neglecting north-south and horizontal effects. The spatial patterns of LOS and vertical subsidence measurements are mainly identical. The similarity demonstrates that the LOS deforming rates are mainly vertical deformation with negligible north-south and horizontal movement.

The average vertical rates of both tracks exhibit similar spatial patterns and magnitude. The average deformation rates in the vertical direction for the two datasets ranged from -97.5 to 10 mm/year. Both eastern and western areas experienced substantial land subsidence. The largest vertical subsidence rate colored in black was detected at -97.5 mm/year in the center of the eastern part near Nazarlu. The subsidence rates decreased gradually to -15 mm/year within a 4 km radius around the area impacted by the maximum subsidence. In the western portion of the study basin near Shendabad, the highest subsidence value that is colored in dark red is -78 mm/year. Most of the study area experienced subsidence ranged from -50 to -30 mm on average each year. The spatial pattern of the subsidence zones is consistent with the distribution of agricultural regions, where have a high dependency on groundwater extraction.

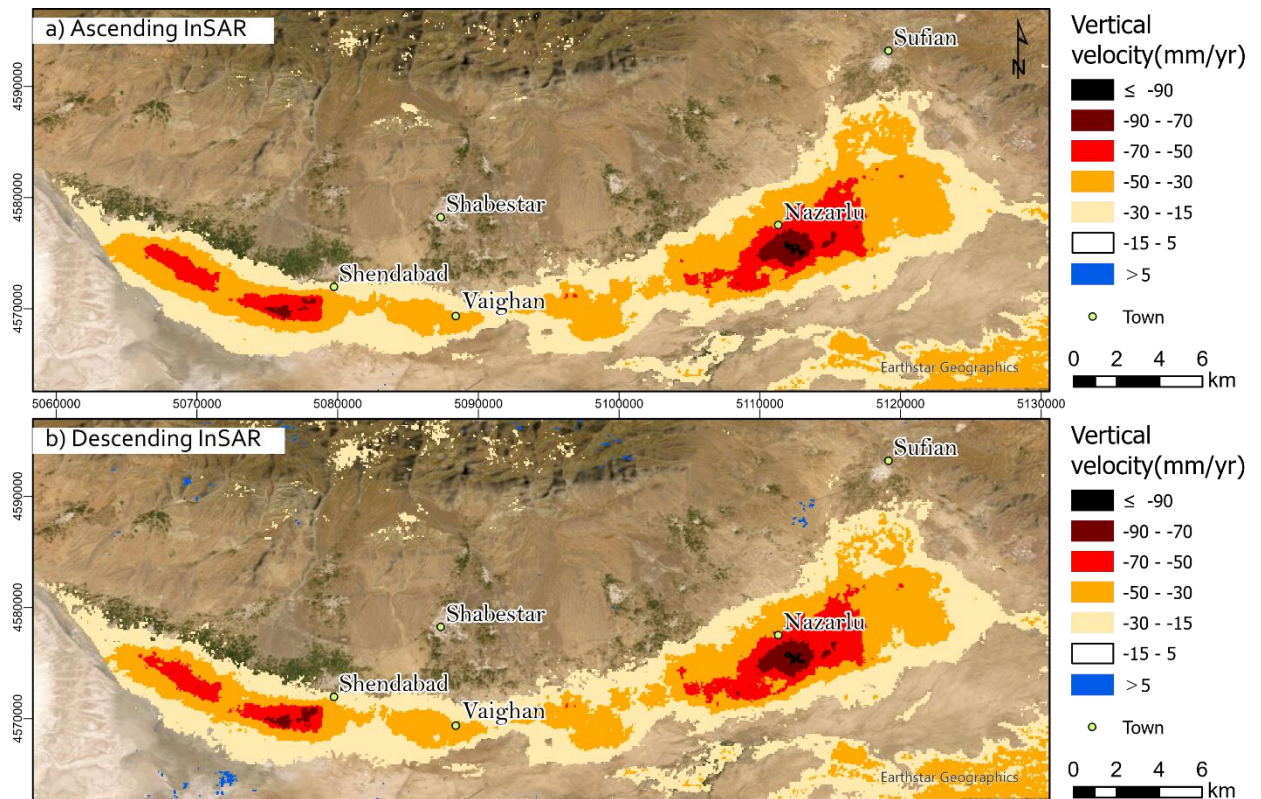


Figure 10. Spatial pattern of mean velocity in a vertical direction from ascending (a) and descending (b) data sets. Areas colored in blue represent uplift movement and negative values denote subsidence.

4.2 Lag correlation

To identify the time lag between the daily subsidence rates and five hydrological variables, ETa, LST, NDVI, P, and SWI, over the period of 2016-2020, the cross-correlation analysis was performed in five deforming zones, where the average subsidence rates were 1) above -90, 2) -90 to -70, 3) -70 to -50, 4) -50 to -30, and 5) -30 to -15 mm/year (Figure 10).

Maximum correlation coefficients over the five years with up to 300 days delay and their corresponding time lags between the five variables and detrended deformation time series are presented in Tables 3 and 4, respectively. Deformation values were multiplied by -1 in order to intuitively present the direct correlation (+) between the subsidence and its driving factors. Subsidence and three variables, including ETa, NDVI, and LST, present positive correlations in five zones, with R_{\max} values of 0.6-0.85. The result revealed that the subsidence increased with increasing ETa, NDVI values, and LST. It is noted that the lag correlation analysis for extracting the time lag

only considered the maximum correlation coefficients between subsidence and the five variables. The importance of different variables is presented in section 4.3. Inverse (-) correlations were identified between the deformation time series and the other two variables: P and SWI (Table 3). The result indicated that subsidence reduced with the increase of P and/or SWI. Nevertheless, these two variables were not considered for predicting land deformation in this thesis, considering the effects of data quality.

The time lags between subsidence occurrence and the five hydrological variables in different zones ranged from 3 to 144 days (Table 4). The time lag between subsidence and LST was the shortest among the three selected variables. The time lag for subsidence responding to LST changes was 54 days in Zone 1, and then increased with the reduction of subsidence rates. The response time for subsidence to NDVI changes ranged between 97 to 122 days. The time lag for NDVI did not show a clear decreasing or increasing trend. The response time between the subsidence and ETa time series was the longest. The time delay started from 106 days in Zone 1 and increased with the decreasing subsidence rates. The time lag between subsidence and SWI time series ranged from 71 to 80 days. In contrast with the previously mentioned four variables, subsidence was not sensitive to precipitation. The time lag between subsidence and precipitation was stable in different zones.

Table 3. Maximum correlation coefficient within a 300-day time frame between the five variables and detrended subsidence time series in five zones during the study period.

R_{max}	ETa	LST	NDVI	P	SWI
(p<0.05)					
z1	0.795	0.858	0.779	-0.318	-0.624
z2	0.769	0.833	0.721	-0.337	-0.593
z3	0.733	0.845	0.766	-0.351	-0.572
z4	0.673	0.844	0.661	-0.374	-0.608
z5	0.627	0.838	0.703	-0.334	-0.620

*z represents zone. p denotes p-values of correlation coefficients. Positive sign shows that the subsidence increases with the increase of the hydrological variables and vice versa.

Table 4. Time lag corresponding to the maximum correlation within a 300-day time frame between the five variables and detrended subsidence time series in five zones during the study period.

Time lag (days)	ETa	LST	NDVI	P	SWI
z1	106	54	122	3	71
z2	109	97	125	3	79
z3	114	97	121	3	79
z4	135	97	110	3	79
z5	144	108	97	3	80

Average subsidence values at each date for each variable in Zone 1 are illustrated in Figure 11. The effect of time shifts for five variables (ETa, LST, NDVI, P, and SWI) was fixed. Seasonal patterns of detrended deformation and five variables can be clearly identified in Figure 12. Positive NDVI, ETa, and LST resulted in negative displacements, or subsidence, in the dry season. Since ETa is defined as a proxy to evaluate groundwater demand, large subsidence (negative number) as a response to an increasing ETa or groundwater extraction was detected between September and October each year. In contrast to subsidence in the dry season, uplift with a slight fluctuation in the wet season was observed due to the positive effect of recharge, possibly due to higher precipitation and the consequent increase in SWI.

It is worth mentioning that the subsidence rate was affected by the spatial distribution of vegetation, as Figure 12 and Figure S1 in Appendix indicate. An increasing NDVI implies a growing groundwater extraction, as the study area's agricultural activities are highly dependent on the groundwater. The higher NDVI values in Zone 1, with subsidence rates below -90 mm/year, were higher than those in the other four zones. Furthermore, the subsidence rate was reduced with decreasing NDVI values. On average, Zone 5 with subsidence rates ranged from -30 to -15 mm/year had the lowest NDVI values relative to NDVI values in the other four zones, which confirms that the subsidence in the area is evidently groundwater driven.

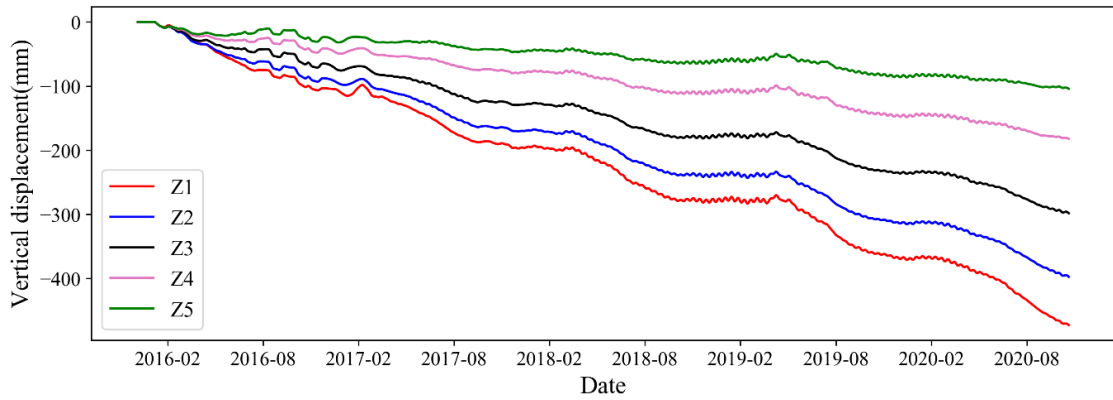


Figure 11. Vertical displacement time series for five zones. The red line represents displacement time series in Zone1 (<-90 mm/year). The pink line denotes cumulative displacement in Zone2 (-90 to -70 mm/year). The black line indicates cumulative displacement in Zone3 (-70 to -50 mm/year). The blue line means cumulative displacement in Zone 4 (-50 to -30 mm/year). The red line represents cumulative displacement in Zone5 (-30 to -15 mm/year).

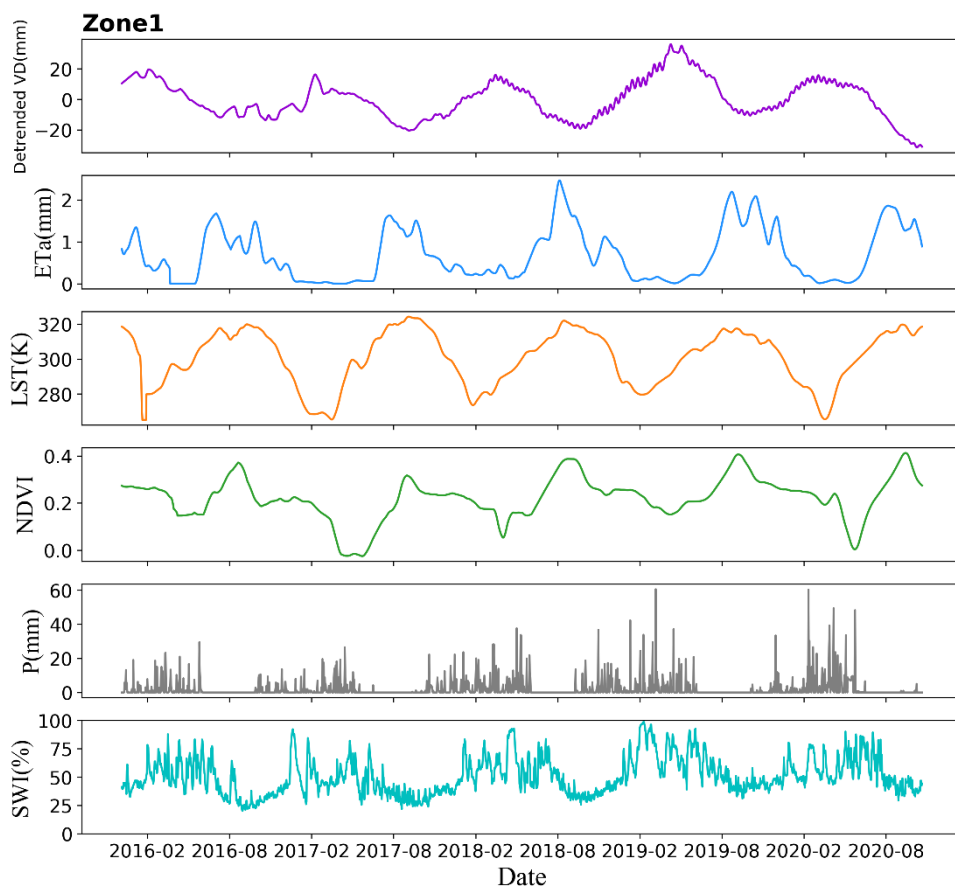


Figure 12. Average values at each date for each variable in Zone 1. Time shifts for five variables (ETa , LST , $NDVI$, P , and SWI) were applied. The purple line represents detrended mean displacement rates. The blue line indicates the actual evapotranspiration (ETa) time series. The yellow line denotes land surface temperature (LST) time series. The green line corresponds to $NDVI$ measurements. The black line stands for precipitation time series. The cyan line represents soil water index (SWI).

4.3 Model evaluation and variable importance

In this section, the importance of three variables encompassing ETa, LST, and NDVI, is presented by implementing LSTM models in different zones. Before performing the entire model, the accuracy of each LSTM prediction model was evaluated using the loss function (Figure 13), which assesses how much the prediction varies from the training results. We subsequently measured RMSE for comparing the differences between the test data and its predicted values in five zones, respectively (Figure 14).

The training loss and validation loss in the five zones showed a downward trend, and both losses were similar and continued to decrease over time (Figure 13s). This reveals that the model is not overfitting. Also, the training loss and validation loss were reduced to near zero after iterating the entire training dataset with 150 epochs. Furthermore, the test data and its predicted value (Figure 14) showed a great agreement with RMSE values of less than 1 in each zone. The result demonstrates that the accuracy of the model is high, lending confidence to the importance of variables and future deformation determined by this model.

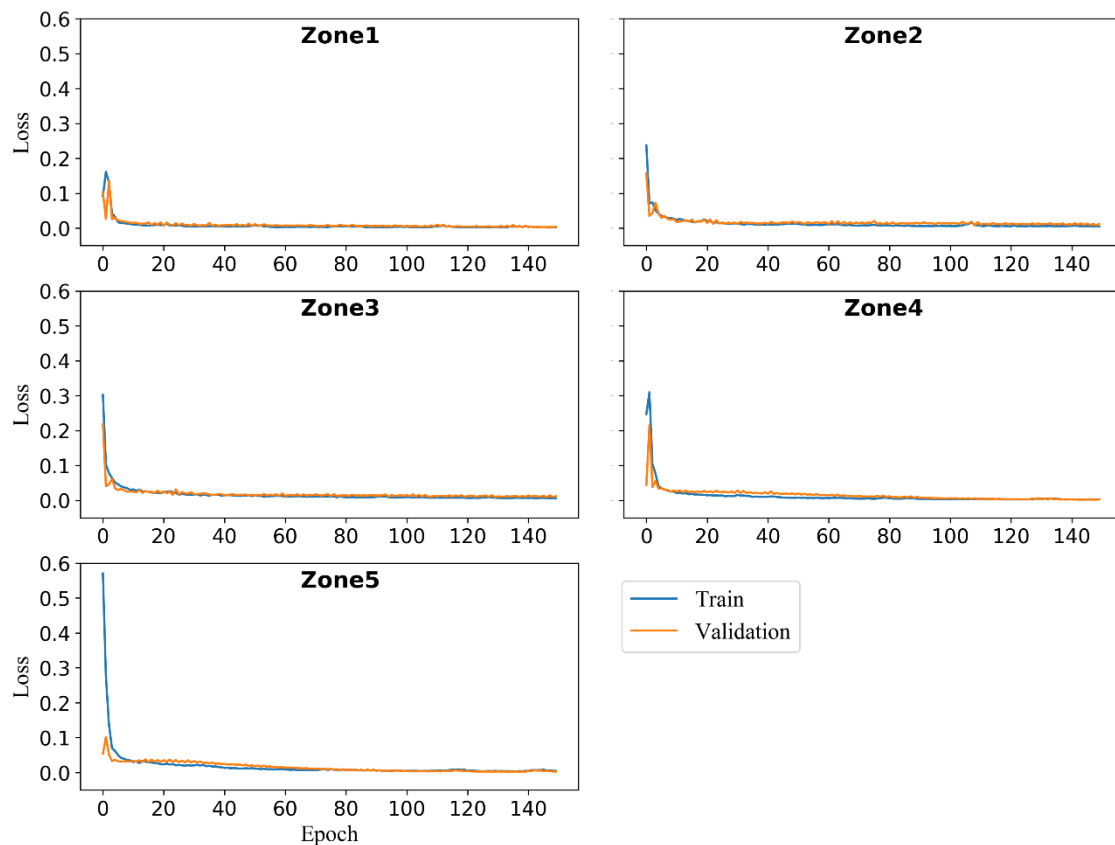


Figure 13. Loss function plots. X-axis in the plot represents the numbers of training epochs. One epoch means iterate the entire training such that each example has been checked once. Y-axis in the plot denotes a summation of errors created for each sample in validation or training phases.

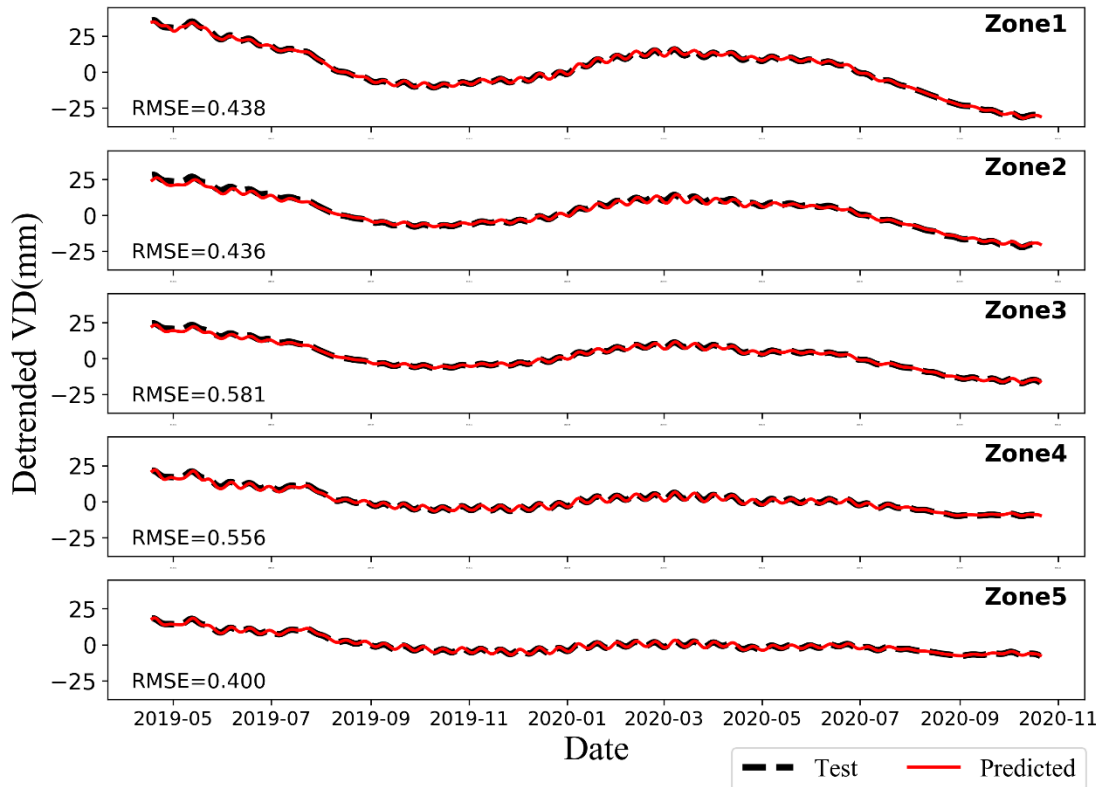
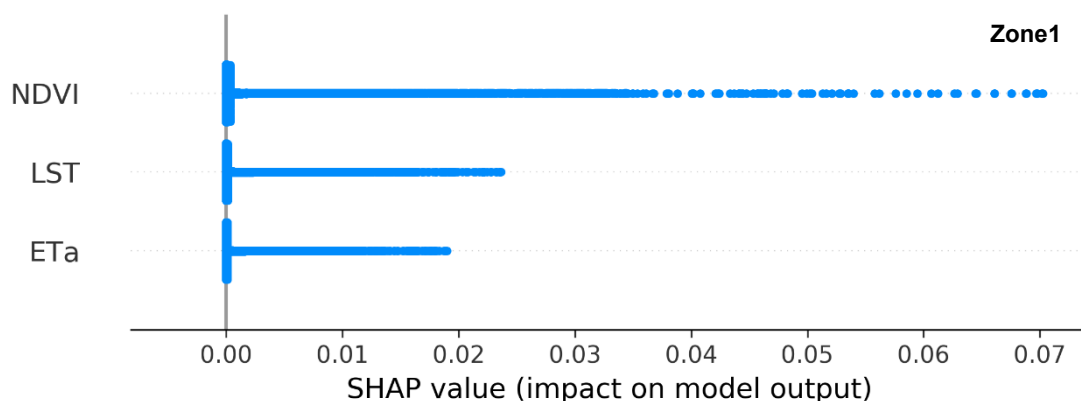


Figure 14. Test dataset vs. predicted values with RMSE values for each zone over time. The black dashed line is the test values, and the red line is the predicted values.

The importance of variables using the SHAP summary plot is illustrated in Figure 15. The NDVI was the most critical variable in predicting subsidence in all zones over the 2016-2020 period based on the model results, except in Zone 4. Even though the most important variable was the ETa in Zone 4, NDVI, ranked the second important variable, having a certain impact on subsidence. LST and ETa had a lower influence on predicting subsidence than NDVI in Zone 1, 3, and 5. A slight discrepancy was found between Zone 2 and these three zones. The impact of ETa on subsidence was marginally higher than those of LST in Zone 2. Overall, despite these slight differences, these results indicate that rates of the vegetated area were the primary variable affecting subsidence.



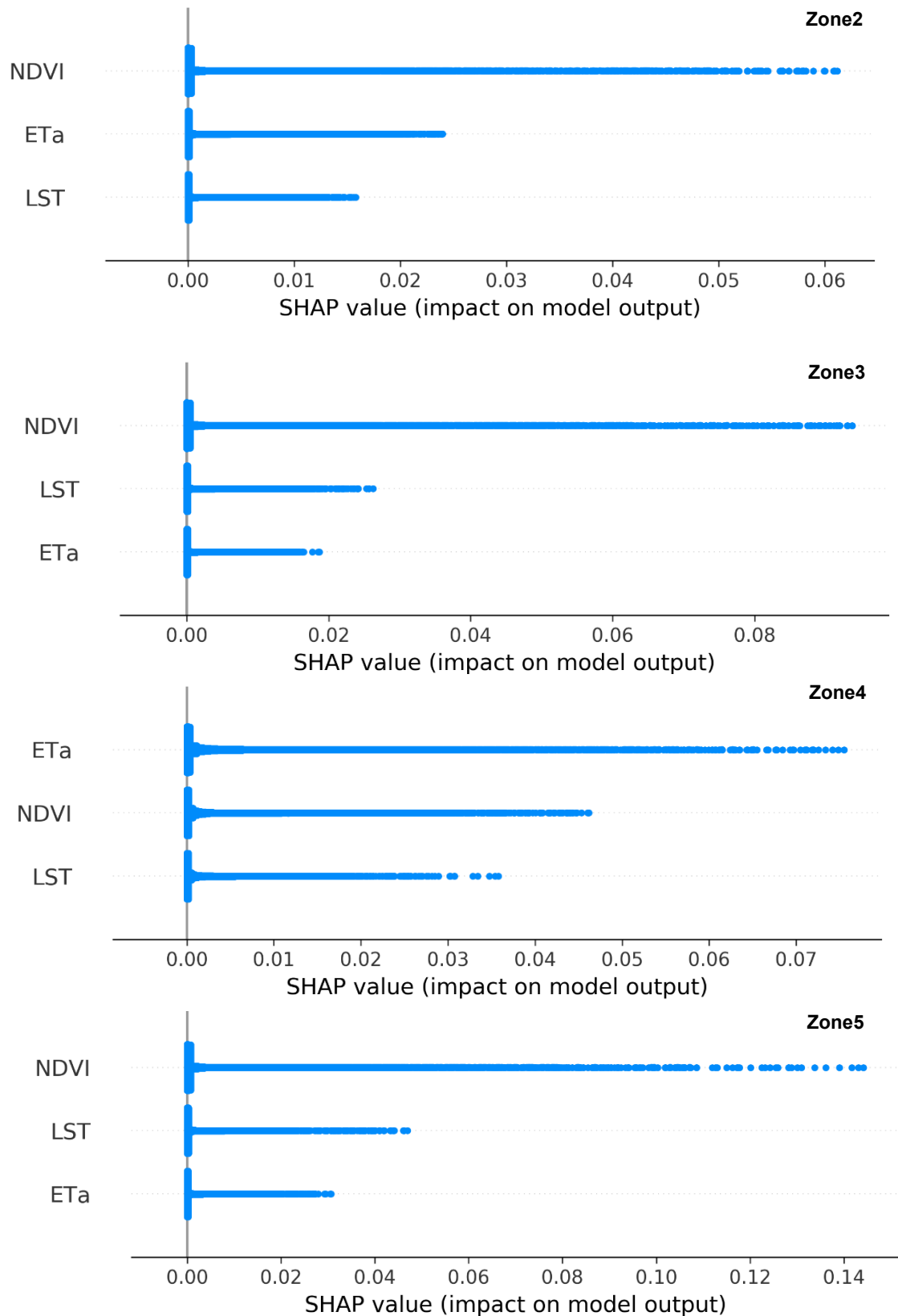


Figure 15. Variable importance charts for each zone created using the SHAP package in Python. These three variables are ranked by mean SHAP values from top to bottom using the built LSTM model.

4.4 Model prediction

Subsidence in the next 1606 days after 21 October 2020 was predicted using the validated LSTM models in five zones. In Zone 1, the subsidence reached -470 mm at the last acquisition date and was estimated to continue increasing in the next 1606 days (Figure 16). The subsidence is projected to reach -856 mm in 2025 without considering other variables such as climate variation and the change in the groundwater management plan. The subsidence was projected to increase by 330 mm reaching to -721 mm in Zone2, and by 240 mm reaching to -542 mm in Zone 3 after 2025. In the Zone 4 and 5, the land is projected to sink up to -327 and -181 mm, respectively.

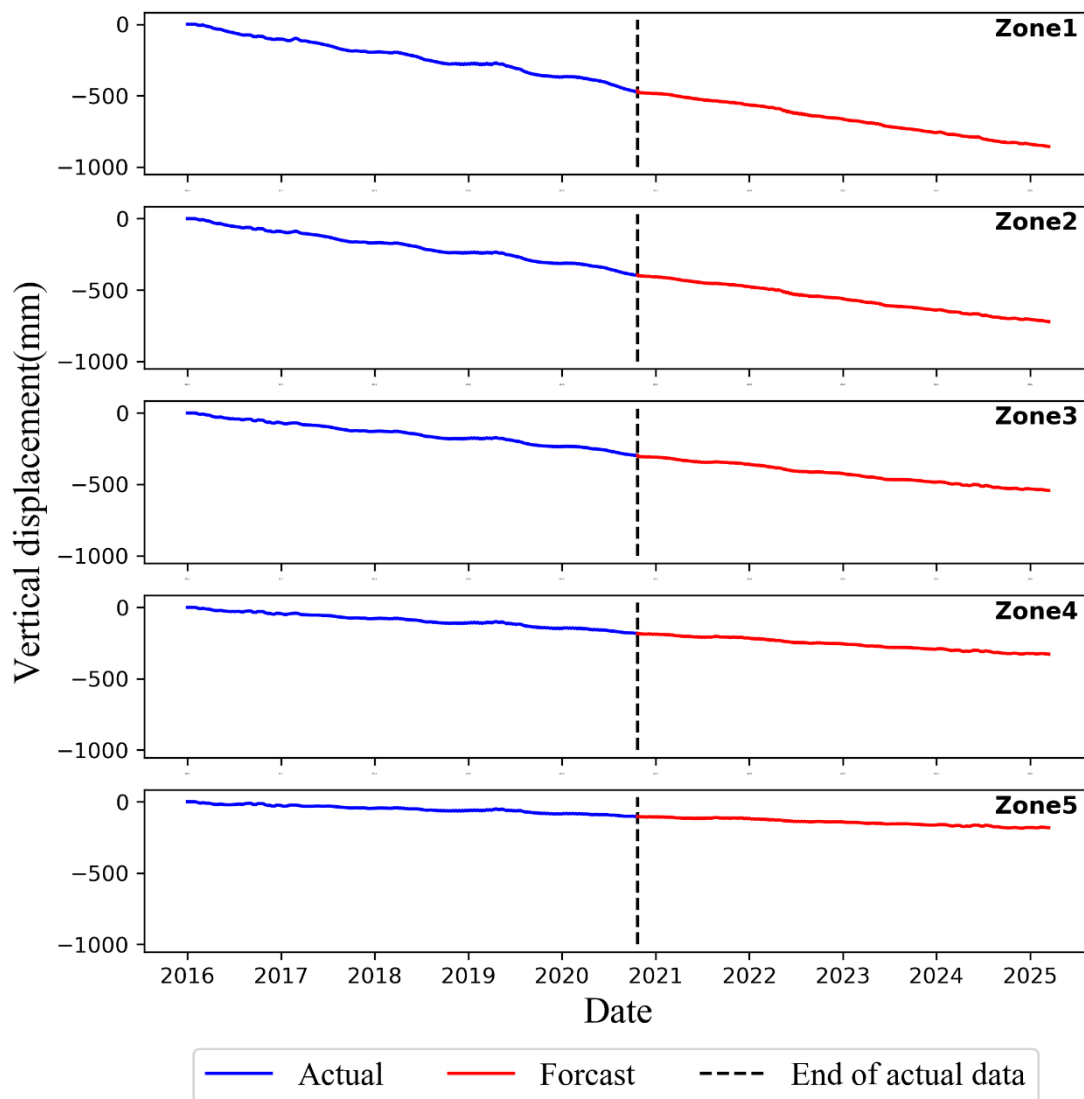


Figure 16. Actual and predicted vertical displacement over the studied time span for each zone. The blue line represents original deformation data. The red line is the predicted values in the next 1606 days. The black dashed line is the border between the actual data and predicted data.

5. Discussion

5.1 Spatial and temporal analysis

The maximum mean subsidence was detected at -97.5 mm/year using the SBAS-InSAR technique with an accuracy of centimeters to sub-centimeters based on the Sentinel-1 data acquired between January 2016 and October 2020. This finding is consistent with that of Nadiri et al. (2018) who demonstrated that the maximum subsidence was -100 mm by normalizing the InSAR ready products with data accuracy of meters between 2015 to 2016. The difference of less than 3 mm is acceptable due to different implemented techniques with varied accuracy. The maximum annual mean subsidence rates based on the data over 2016-2020 were detected in the eastern part of the basin near Nazarlu, while the previous paper showed the subsidence observed near the town ranged from -50 to -25 mm in 2015-2016. Despite the fact that inconsistency was found between the current study and the previous research, our study is more reliable since we processed both ascending and descending data; furthermore, evidence in the prior study indicated the eastern area had the highest vulnerability, and the risk exposure to subsidence was likely accelerating. In the current paper, a large subsidence signature (-90 to -50 mm/year) was also detected in the westernmost of the basin close to Lake Urmia similar to the previous paper. This accords with observations in the previous study, which showed subsidence was -100 to -50 mm in the studied year in the western basin, where the subsidence vulnerability was estimated to be moderate.

The shape and the location of the subsidence pattern are consistent with the spatial distribution of the agricultural region, which mainly relies on groundwater extraction. Seasonal fluctuations in subsidence were found in the study area. These commonly result from a high irrigation water extraction during dry seasons and a decreased extraction during wet seasons. The subsidence pattern suggests that subsidence is majorly affected by human activity.

Hydrological variables considered in the current study, including ETa, NDVI, LST, P, and SWI, reflect the potential impact of irrigated water demand, which triggers subsidence in the area. The estimated varied time lag between these variables and subsidence time series in different zones with different subsidence rates reveals that

the aquifer thickness also affects the subsidence rates. As mentioned in the literature review section, the maximum aquifer thickness occurs in the eastern portion of the study area near Nazarlu, and the thickness decrease in all directions from this place. The area with the maximum thickness dominated by clay and silt is prone to subsidence. This results in a shorter response time to groundwater table changes in the area than that in places dominated by sand and gravel. The phenomenon is explicitly reflected in lag correlation analysis between the ETa, SWI, and land deformation.

The current study demonstrated a meaningful correlation between the subsidence and driving factors. In contrast to these findings, the correlation between subsidence and P and SWI time series was weaker than that of the other three variables. The result indicated that these two variables do not have considerable impacts on subsidence; furthermore, the finding reflects that precipitation and soil moisture have a weak influence on the resilience of groundwater in the study area. It is worth mentioning that NDVI values in zones with substantial subsidence signature were higher than those in zones with low subsidence signature. The spatial pattern and the correlation analysis in the studied time span demonstrated that agricultural water extraction has a massive impact on subsidence.

The importance of variables over 2016-2020 was performed using the LSTM model. NDVI, which reflects NDVI values, greatly affected subsidence in each zone, except Zone 4, with the subsidence rate ranged from -50 to -30 mm/year. Despite the fact that NDVI was not the primary variable that affected subsidence in Zone 4, NDVI was ranked the second still substantially driving subsidence rate. This discrepancy could be attributed to the higher spatial distribution of subsidence in Zone 4. Most of the study area experienced subsidence ranged from -50 to -30 mm/year (Zone 4). The average values at each date for this zone were possibly influenced by spatial heterogeneity resulting from temporal decorrelation affected by vegetation growth. Despite the inconsistency, LST and ETa had less impact on subsidence than NDVI in the other four zones. These findings quantitatively reveal that irrigation agriculture had a massive impact on land subsidence in the basin.

5.2 Data

As previously stated, the LSTM model with SBAS-InSAR-derived vertical displacement and hydrological variables achieved a good performance. The InSAR-derived LOS deformation from ascending and descending data sets remained a discrepancy in quantitative analysis. The differences could stem from atmospheric effects, different temporal coverage, looking geometries, phase unwrapping, seasonal biases, and temporal decorrelation. The vegetated area with low coherence resulted in noise on interferograms, which led to unwrapping errors and inconsistency between ascending and descending derived displacement. The deformation derived using the SBAS technique, which has the advantage of mitigating decorrelation phenomena, might require GPS data to adjust possible biases and errors. For this reason, it is essential to establish GSP stations in the study area for time-series deformation measurement and the validation of SBAS analysis or other techniques such as PS-InSAR in the future.

The InSAR-derived data were detrended to comply with the assumption of being independent. The study assumed that the data followed a linear trend. Despite the nonlinear phenomena that may result from an uneven temporal coverage of InSAR-derived rates from two different data sets, a prior study by Yang et al. (2019) still removed a linear trend from InSAR-derived velocities for seasonal analysis and achieved a positive result for evaluating relationships between seasonal groundwater variation and precipitation. The accuracy of InSAR-derived data for the correlation analysis can be improved by removing the nonlinear trend of the data. However, the measurement of the nonlinear trend for the massive number of data requires large computer expenses and a long execution time.

Satellite products of hydrological variables, including ETa, LST, NDVI, P, and SWI, were harmonized to daily data with the spatial resolution of InSAR-derived displacements. Satellite data from EEFflux with an initial spatial resolution of 30 m required a gap-fill in the time series. Even though the accuracy of the interpolated daily data may be controversial, the availability and quality of ground-truth data were problematic. Daily satellite products, including P and SWI, which possibly affected subsidence, with fine resolutions, were not used in the model after testing the lag correlation between these variables and subsidence time series. Quantitatively

evaluating potential variables affecting subsidence is challenging in the area with inadequate ground-truth data. For this reason, the current study only conducts an approximation of variable importance with satellite products. Ground-truth data was also essential in future studies to improve the accuracy of the estimation at the local scale. However, this study proves the high potential of satellite-based hydrological variables in subsidence investigation in data-poor regions.

5.3 Model

The present study implemented a deep learning approach to estimate the importance of hydrological variables that potentially drive the subsidence phenomenon. The model was subsequently used to predict future subsidence. As explained in the result, the model achieved an excellent performance. There is abundant space for further progress in predicting subsidence to assist future groundwater management using deep learning algorithms. Due to the limitation of station data and spatial resolution of P and SWI products, the model only considered three variables: ETa, LST, and NDVI. Sediment compressibility and sediment thickness can also be considered as input variables for modeling subsidence if ground-truth data are available. According to Equation 9 mentioned in the background, the total land deformation is proportional to the sediment thickness (b) and the skeletal specific storage (S_{sk}). The basin is dominated by alluvial deposits, consisting of clay and silt in the east and the west. This makes the aquifer highly prone to subsidence under excessive pumping. In addition, aquifer thickness also affects subsidence rates, as discussed early in section 5.1. Considering these two variables in a future model is therefore suggested.

The LSTM model is highly dependent upon the historical data sets. This indicates that the model in each zone can only predict subsidence in the next 1606 days since the training data and test data were 60 and 40% of the data set containing 903 and 553 days, respectively, with 150 time steps. In future studies, it might be possible to use data with wide temporal coverage for predicting subsidence in the next ten years.

We established five models for different zones with varying magnitudes of subsidence to avoid bias in higher or lower subsiding areas. However, only mean values were considered in the model for each zone. The model may be biased if there is spatial heterogeneity in an area. Future research should be undertaken to evaluate the

performance of the model on each pixel in different zones to improve the accuracy of the model.

5.4 Future groundwater management

The motivation of the study is to investigate the relationship between hydrological variables and subsidence in order to inform groundwater management. The study demonstrated that agricultural activity is the primary variable that affects subsidence. In addition, the subsidence is predicted to continue increasing in the next 1606 days without considering groundwater management change and climate variability in future. The agricultural area is at high risk of being affected by subsidence. The most vulnerable area near Nazarlu is projected to continue subsiding by around 386 mm by 2025. The continuing subsidence will result in local economic losses and poses a high risk to human lives. For these reasons, the study suggests implementing regional governance: Regulating human activities and improving agricultural water-use efficiency, particularly in the zone with an intensive risk of being influenced by subsidence.

In addition to human activity, climate change could also affect groundwater storage (Wu et al. 2020). The paper by Wu et al. 2020 also demonstrated that the effect of groundwater decline could easily far exceed the climatic change impact. In future investigations, it might be possible to consider climate change scenarios in the model to assist groundwater management and work towards water resources sustainability.

6. Conclusion

The study characterized and evaluated land deformation from 2016 to 2020 using the SBAS-InSAR technique. Spatial patterns with the use of both ascending and descending tracks exhibited good agreement, although the InSAR-derived LOS deformation from ascending and descending data sets showed a minimal discrepancy in quantitative analysis. The SBAS-InSAR technique was influenced by low coherence in the vegetated area. There is abundant room for further progress in improving the accuracy of InSAR-derived ground deformation in agricultural regions.

We identified land subsidence at rates ranging from -97.5 to 10 mm/year after decomposing InSAR LOS displacement to vertical components. The maximum subsidence was found in the eastern part of the basin near Nazarlu, where the alluvium aquifer mainly contains clay and silt. The shape and the location of the subsidence pattern were consistent with the spatial distribution of the agricultural lands, which primarily rely on groundwater supply.

The current study demonstrated that the increased ETa, LST, and NDVI values resulted in negative vertical displacement or subsidence. Future studies will include five variables and improve data quality.

The LSTM model with SBAS-InSAR-derived vertical displacement and hydrological variables achieved a good performance. The importance of variables over 2016-2020 in zones with varying subsidence rates was ranked using the LSTM model. All these findings quantitatively revealed that agricultural activity is the primary variable causing subsidence. The model can be improved by considering the sediment texture and thickness in combination with in-situ measurements.

The subsidence phenomenon was projected to continue in the next 1606 days. Our findings recommend regulating agricultural activities, improving water use efficiency, and working toward water resources sustainability.

7. Reference

- Allen, R. G., C. Morton, B. Kamble, A. Kilic, J. Huntington, D. Thau, N. Gorelick, T. Erickson, et al. 2015. EEFlux: A Landsat-based evapotranspiration mapping tool on the Google Earth Engine. In *2015 ASABE/IA Irrigation Symposium: Emerging Technologies for Sustainable Irrigation-A Tribute to the Career of Terry Howell, Sr. Conference Proceedings*: American Society of Agricultural and Biological Engineers, 1-11.
- Allen, R. G., M. Tasumi, A. Morse, R. Trezza, J. L. Wright, W. Bastiaanssen, W. Kramber, I. Lorite, et al. 2007a. Satellite-based energy balance for mapping evapotranspiration with internalized calibration (METRIC)—Applications. *Journal of irrigation and drainage engineering*, 133: 395-406.
- Allen, R. G., M. Tasumi, and R. Trezza. 2007b. Satellite-based energy balance for mapping evapotranspiration with internalized calibration (METRIC)—Model. *Journal of irrigation and drainage engineering*, 133: 380-394.
- Bamler, R., and P. Hartl. 1998. Synthetic aperture radar interferometry. *Inverse problems*, 14: R1.
- Baran, I., M. P. Stewart, B. M. Kampes, Z. Perski, and P. Lilly. 2003. A modification to the Goldstein radar interferogram filter. *IEEE Transactions on Geoscience and Remote Sensing*, 41: 2114-2118.
- Bauer-Marschallinger, B., C. Paulik, S. Hochstöger, T. Mistelbauer, S. Modanesi, L. Ciabatta, C. Massari, L. Brocca, et al. 2018. Soil moisture from fusion of scatterometer and SAR: Closing the scale gap with temporal filtering. *Remote Sensing*, 10: 1030.
- Béjar-Pizarro, M., P. Ezquerro, G. Herrera, R. Tomás, C. Guardiola-Albert, J. M. R. Hernández, J. A. F. Merodo, M. Marchamalo, et al. 2017. Mapping groundwater level and aquifer storage variations from InSAR measurements in the Madrid aquifer, Central Spain. *Journal of Hydrology*, 547: 678-689.
- Berardino, P., G. Fornaro, R. Lanari, and E. Sansosti. 2002. A new algorithm for surface deformation monitoring based on small baseline differential SAR interferograms. *IEEE Transactions on geoscience and remote sensing*, 40: 2375-2383.
- Brocca, L., F. Melone, T. Moramarco, W. Wagner, and S. Hasenauer. 2010. ASCAT soil wetness index validation through in situ and modeled soil moisture data in central Italy. *Remote Sensing of Environment*, 114: 2745-2755.
- Castellazzi, P., R. Martel, D. L. Galloway, L. Longuevergne, and A. Rivera. 2016. Assessing groundwater depletion and dynamics using GRACE and InSAR: Potential and limitations. *Groundwater*, 54: 768-780.
- Center for Hydrometeorology and Remote Sensing (CHRS). 2016-2020. PERSIANN-Cloud Classification System (CCS) global satellite precipitation data. Retrieved 10 February 2021 from The CHRS Data Portal: <https://chrsdata.eng.uci.edu/>.
- Committee on Earth Observation Satellites(CEOS). *The CEOS Earth Observation*

- (EO) *Handbook-Catalogue of satellite instruments*. The European Space Agency.
- Chaussard, E., R. Bürgmann, M. Shirzaei, E. J. Fielding, and B. Baker. 2014. Predictability of hydraulic head changes and characterization of aquifer-system and fault properties from InSAR-derived ground deformation. *Journal of Geophysical Research: Solid Earth*, 119: 6572-6590.
- Chen, C. W., and H. A. Zebker. 2002. Phase unwrapping for large SAR interferograms: Statistical segmentation and generalized network models. *IEEE Transactions on Geoscience and Remote Sensing*, 40: 1709-1719.
- Chen, J., R. Knight, and H. A. Zebker. 2017. The temporal and spatial variability of the confined aquifer head and storage properties in the San Luis Valley, Colorado inferred from multiple InSAR missions. *Water Resources Research*, 53: 9708-9720.
- Copernicus Global Land Operations. 2019. *Product User Manual Soil Water Index 1km V1*. Retrieved 25 March 2021, from Available: https://land.copernicus.eu/global/sites/cgls.vito.be/files/products/CGLOPS1_PUM_SW11km-V1_I1.10.pdf
- Crosetto, M., O. Monserrat, M. Cuevas-González, N. Devanthéry, and B. Crippa. 2016. Persistent Scatterer Interferometry: A review. *ISPRS Journal of Photogrammetry and Remote Sensing*, 115: 78-89. DOI: 10.1016/j.isprsjprs.2015.10.011
- de Oliveira Costa, J., J. V. José, W. Wolff, N. P. R. de Oliveira, R. C. Oliveira, N. L. Ribeiro, R. D. Coelho, T. J. A. da Silva, et al. 2020. Spatial variability quantification of maize water consumption based on Google EEflux tool. *Agricultural Water Management*, 232: 106037.
- De Zan, F., and A. M. Guarnieri. 2006. TOPSAR: Terrain observation by progressive scans. *IEEE Transactions on Geoscience and Remote Sensing*, 44: 2352-2360.
- Döll, P. 2009. Vulnerability to the impact of climate change on renewable groundwater resources: a global-scale assessment. *Environmental Research Letters*, 4: 035006.
- Döll, P., H. Mueller Schmied, C. Schuh, F. T. Portmann, and A. Eicker. 2014. Global-scale assessment of groundwater depletion and related groundwater abstractions: Combining hydrological modeling with information from well observations and GRACE satellites. *Water Resources Research*, 50: 5698-5720.
- East Azerbaijan Regional Water Authority, 2015. Private Transactions with East Azerbaijan Regional Water Authority to Obtain Data
- Eftekharnejad, J., Gharashi, M., Mehrparto, M., Arshadi, S., Zohrehbakhsh, A., 2000. Geological map of Tabriz-Poldasht (1:250000). *Geological Survey & Mineral Exploration of Iran*.
- Esri, GEBCO, NOAA, National Geographic, DeLorme, HERE, Geonames.org, and other contributors. 2011. The World Ocean Basemap(~1:288,000). Retrieved 25 March 2021, from https://services.arcgisonline.com/ArcGIS/rest/services/Ocean_Basemap/MapS

erver.

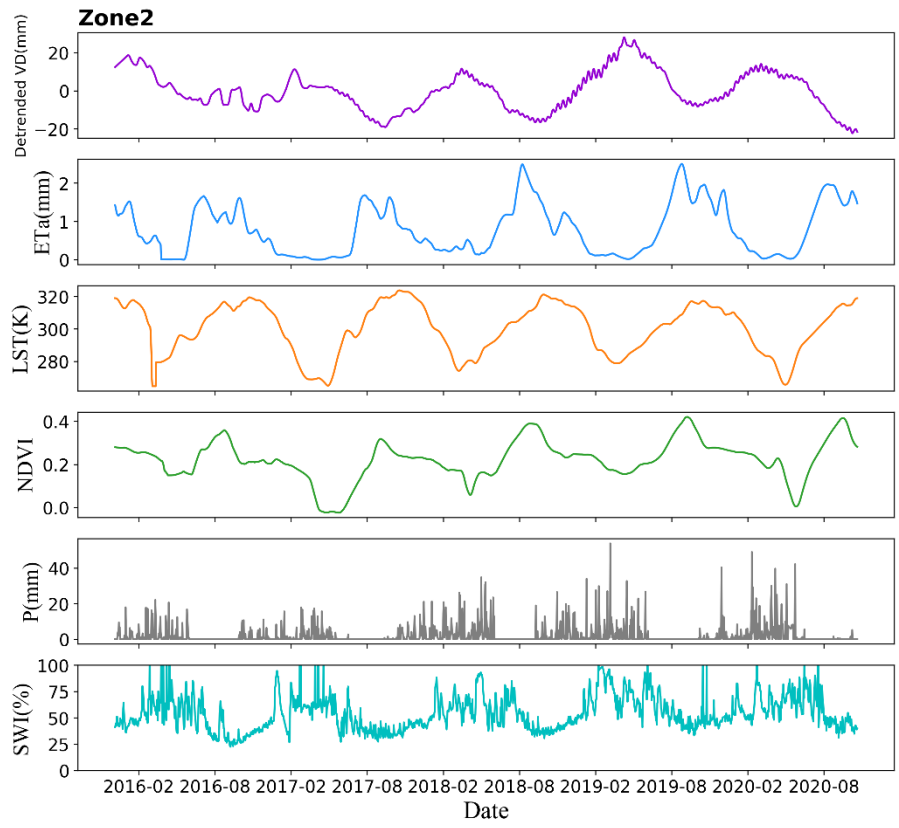
- Esri, Airbus DS, USGS, NGA, NASA, CGIAR, N Robinson, NCEAS, NLS, OS, NMA, Geodatastyrelsen, Rijkswaterstaat, GSA, Geoland, FEMA, Intermap, and the GIS user community. 2018. The World Hillshade(~1:577,000). Retrieved 25 March 2021, from https://tiledbasemaps.arcgis.com/arcgis/rest/services/Elevation/World_Hillshade/MapServer.
- Ferrant, S., Y. Caballero, J. Perrin, S. Gascoin, B. Dewandel, S. Aulong, F. Dazin, S. Ahmed, et al. 2014. Projected impacts of climate change on farmers' extraction of groundwater from crystalline aquifers in South India. *Scientific reports*, 4: 1-10.
- Ferretti, A., C. Prati, and F. Rocca. 2000. Nonlinear subsidence rate estimation using permanent scatterers in differential SAR interferometry. *IEEE Transactions on geoscience and remote sensing*, 38: 2202-2212.
- Ferretti, A., C. Prati, and F. Rocca. 2001. Permanent scatterers in SAR interferometry. *IEEE Transactions on Geoscience and Remote Sensing*, 39: 8-20. DOI: 10.1109/36.898661
- Goldstein, R., and C. Werner. 1997. Radar ice motion interferometry.
- Goldstein, R. M., H. A. Zebker, and C. L. Werner. 1988. Satellite radar interferometry: Two-dimensional phase unwrapping. *Radio Science*, 23: 713-720. DOI: 10.1029/RS023i004p00713
- Hochreiter, S., and J. Schmidhuber. 1997. Long Short-Term Memory. *Neural Computation*, 9: 1735-1780. DOI: 10.1162/neco.1997.9.8.1735
- Hoffmann, J., H. A. Zebker, D. L. Galloway, and F. Amelung. 2001. Seasonal subsidence and rebound in Las Vegas Valley, Nevada, observed by synthetic aperture radar interferometry. *Water Resources Research*, 37: 1551-1566.
- Hong, Y., K.-L. Hsu, S. Sorooshian, and X. Gao. 2004. Precipitation estimation from remotely sensed imagery using an artificial neural network cloud classification system. *Journal of Applied Meteorology*, 43: 1834-1853.
- Jiang, L., L. Bai, Y. Zhao, G. Cao, H. Wang, and Q. Sun. 2018. Combining InSAR and hydraulic head measurements to estimate aquifer parameters and storage variations of confined aquifer system in Cangzhou, North China Plain. *Water Resources Research*, 54: 8234-8252.
- Karbalae, N., K. Hsu, S. Sorooshian, and D. Braithwaite. 2017. Bias adjustment of infrared-based rainfall estimation using passive microwave satellite rainfall data. *Journal of Geophysical Research: Atmospheres*, 122: 3859-3876.
- Lundberg, S. M., and S. I. Lee. 2017. A unified approach to interpreting model predictions. red. I. Guyon, R. Fergus, H. Wallach, H. Wallach, I. Guyon, S. V. N. Vishwanathan, U. von Luxburg, R. Garnett, S. V. N. Vishwanathan, S. Bengio, and R. Fergus: Neural information processing systems foundation, 4766-4775.
- Mayes, M., K. K. Caylor, M. B. Singer, J. C. Stella, D. Roberts, and P. Nagler. 2020. Climate sensitivity of water use by riparian woodlands at landscape scales. *Hydrological Processes*, 34: 4884-4903.

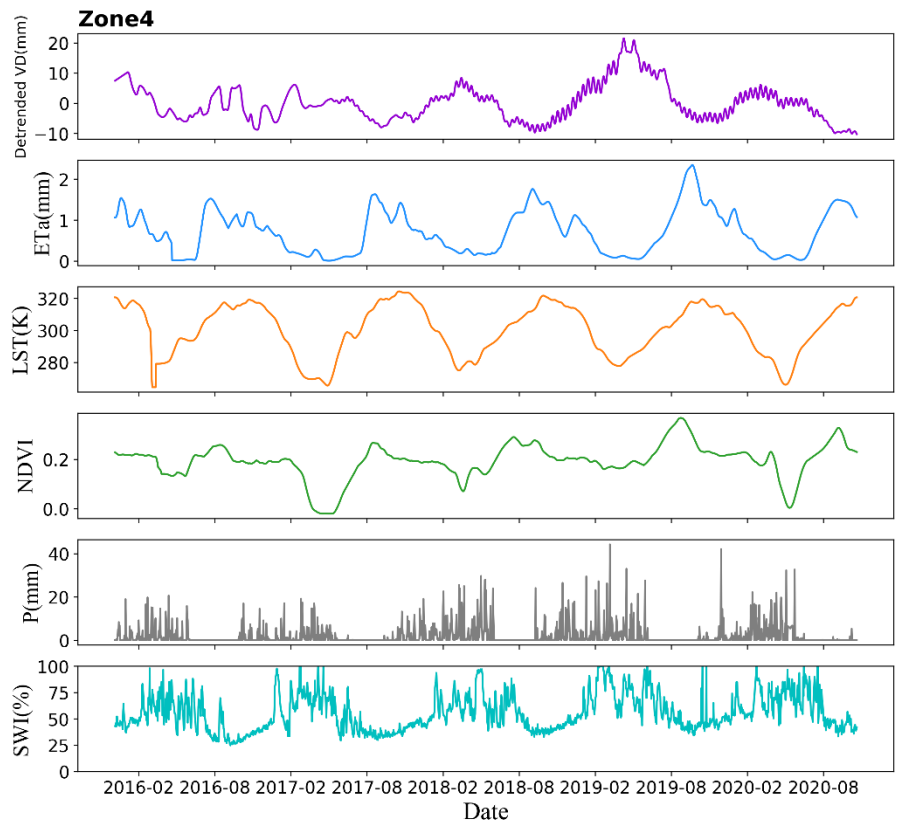
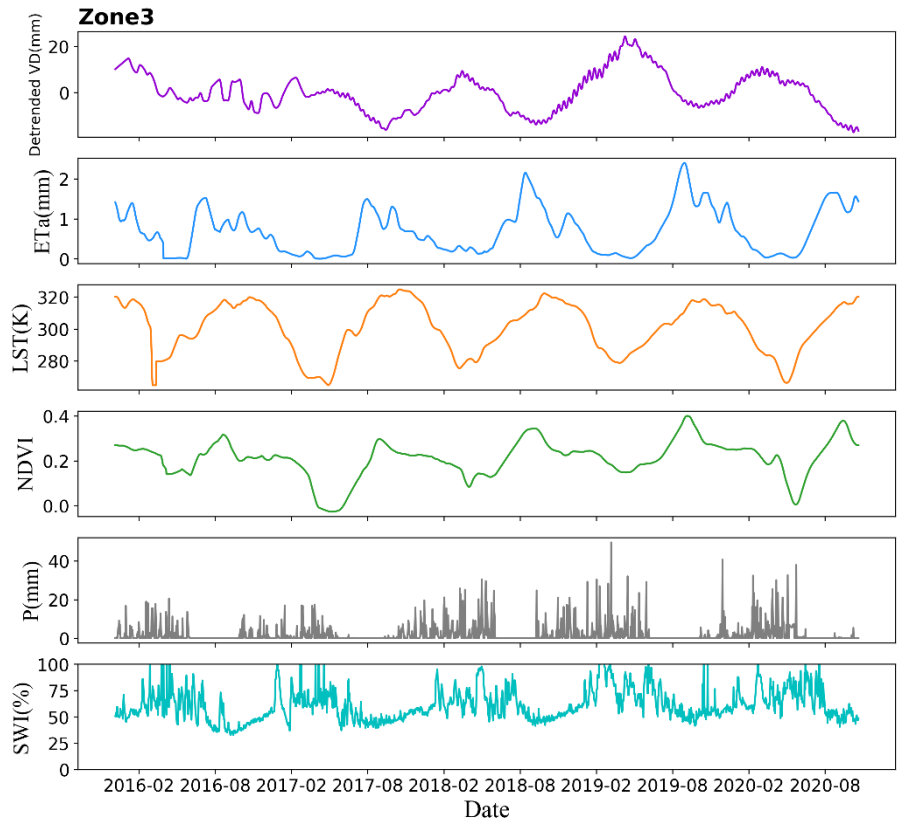
- Mehr, S. S., A. A. Moghaddam, and M. S. Field. 2019. Hydrogeological and geochemical evidence for the origin of brackish groundwater in the Shabestar plain aquifer, northwest Iran. *Sustainable Water Resources Management*, 5: 1381-1404.
- Miller, M. M., M. Shirzaei, and D. Argus. 2017. Aquifer mechanical properties and decelerated compaction in Tucson, Arizona. *Journal of Geophysical Research: Solid Earth*, 122: 8402-8416.
- Moazami, S., S. Golian, Y. Hong, C. Sheng, and M. R. Kavianpour. 2016. Comprehensive evaluation of four high-resolution satellite precipitation products under diverse climate conditions in Iran. *Hydrological Sciences Journal*, 61: 420-440.
- Moreira, A., P. Prats-Iraola, M. Younis, G. Krieger, I. Hajnsek, and K. P. Papathanassiou. 2013. A tutorial on synthetic aperture radar. *IEEE Geoscience and remote sensing magazine*, 1: 6-43.
- Mosaffa, H., A. Shirvani, D. Khalili, P. Nguyen, and S. Sorooshian. 2020. Post and near real-time satellite precipitation products skill over Karkheh River Basin in Iran. *International Journal of Remote Sensing*, 41: 6484-6502.
- Motagh, M., R. Shamshiri, M. H. Haghighi, H.-U. Wetzel, B. Akbari, H. Nahavandchi, S. Roessner, and S. Arabi. 2017. Quantifying groundwater exploitation induced subsidence in the Rafsanjan plain, southeastern Iran, using InSAR time-series and in situ measurements. *Engineering Geology*, 218: 134-151.
- Nadiri, A. A., Z. Taheri, R. Khatibi, G. Barzegari, and K. Dideban. 2018. Introducing a new framework for mapping subsidence vulnerability indices (SVIs): ALPRIFT. *Science of the Total Environment*, 628: 1043-1057.
- National Aeronautics and Space Administration(NASA) Jet Propulsion Laboratory (JPL). 2013. NASA Shuttle Radar Topography Mission Global 3 arc second. Retrieved 10 November 2021 from <http://www2.jpl.nasa.gov/srtm/>.
- Ojha, C., M. Shirzaei, S. Werth, D. F. Argus, and T. G. Farr. 2018. Sustained groundwater loss in California's Central Valley exacerbated by intense drought periods. *Water resources research*, 54: 4449-4460.
- Oliver, C., and S. Quegan. 2004. *Understanding synthetic aperture radar images*. SciTech Publishing.
- Paulik, C., W. Dorigo, W. Wagner, and R. Kidd. 2014. Validation of the ASCAT Soil Water Index using in situ data from the International Soil Moisture Network. *International journal of applied earth observation and geoinformation*, 30: 1-8.
- Press, W. H., S. A. Teukolsky, W. T. Vetterling, and B. P. Flannery. 1992. Numerical recipes in C++. *The art of scientific computing*, 2: 1002.
- Pringle, M., M. Schmidt, and J. Muir. 2009. Geostatistical interpolation of SLC-off Landsat ETM+ images. *ISPRS Journal of Photogrammetry and Remote Sensing*, 64: 654-664.
- Richey, A. S., B. F. Thomas, M. H. Lo, J. S. Famiglietti, S. Swenson, and M. Rodell. 2015a. Uncertainty in global groundwater storage estimates in a Total Groundwater Stress framework. *Water resources research*, 51: 5198-5216.

- Richey, A. S., B. F. Thomas, M. H. Lo, J. T. Reager, J. S. Famiglietti, K. Voss, S. Swenson, and M. Rodell. 2015b. Quantifying renewable groundwater stress with GRACE. *Water resources research*, 51: 5217-5238.
- Rodell, M., J. Chen, H. Kato, J. S. Famiglietti, J. Nigro, and C. R. Wilson. 2007. Estimating groundwater storage changes in the Mississippi River basin (USA) using GRACE. *Hydrogeology Journal*, 15: 159-166.
- Rosen, P. A., S. Hensley, I. R. Joughin, F. K. Li, S. N. Madsen, E. Rodriguez, and R. M. Goldstein. 2000. Synthetic aperture radar interferometry. *Proceedings of the IEEE*, 88: 333-382.
- Salgado, R., and L. Mateos. 2021. Evaluation of different methods of estimating ET for the performance assessment of irrigation schemes. *Agricultural Water Management*, 243: 106450.
- Sandwell, D., R. Mellors, X. Tong, M. Wei, and P. Wessel. 2011a. GMTSAR: An insar processing system based on generic mapping tools.
- Sandwell, D., R. Mellors, X. Tong, M. Wei, and P. Wessel. 2011b. Open radar interferometry software for mapping surface deformation. Wiley Online Library.
- Scanlon, B. R., L. Longuevergne, and D. Long. 2012. Ground referencing GRACE satellite estimates of groundwater storage changes in the California Central Valley, USA. *Water Resources Research*, 48.
- Scanlon, B. R., Z. Zhang, H. Save, D. N. Wiese, F. W. Landerer, D. Long, L. Longuevergne, and J. Chen. 2016. Global evaluation of new GRACE mascon products for hydrologic applications. *Water Resources Research*, 52: 9412-9429.
- Siami-Namini, S., N. Tavakoli, and A. S. Namin. 2018. A comparison of ARIMA and LSTM in forecasting time series. In *2018 17th IEEE International Conference on Machine Learning and Applications (ICMLA)*: IEEE, 1394-1401.
- Smith, R. G., R. Knight, J. Chen, J. Reeves, H. Zebker, T. Farr, and Z. Liu. 2017. Estimating the permanent loss of groundwater storage in the southern San Joaquin Valley, California. *Water Resources Research*, 53: 2133-2148.
- Sorooshian, S., K.-L. Hsu, X. Gao, H. V. Gupta, B. Imam, and D. Braithwaite. 2000. Evaluation of PERSIANN system satellite-based estimates of tropical rainfall. *Bulletin of the American Meteorological Society*, 81: 2035-2046.
- The Copernicus Global Land Service (CGLS). 2016-2020. Sentinel-1 C-SAR and Metop ASCAT. Retrieved 10 February 2021 from The CGLS Data Portal.
- The European Space Agency(ESA). 2016-2020. Copernicus Sentinel data. Retrieved 10 November 2021 from <https://scihub.copernicus.eu/>, processed by ESA.
- The European Space Agency(ESA). 2016-2020. Copernicus Precise Orbit Determination (POD) data. Retrieved 10 November 2021 from Alaska Satellite Facility (ASF) DAAC, processed by ESA.
- Torres, R., P. Snoeij, D. Geudtner, D. Bibby, M. Davidson, E. Attema, P. Potin, B. Rommen, et al. 2012. GMES Sentinel-1 mission. *Remote Sensing of Environment*, 120: 9-24.
- Velis, M., K. I. Conti, and F. Biermann. 2017. Groundwater and human development:

- synergies and trade-offs within the context of the sustainable development goals. *Sustainability science*, 12: 1007-1017.
- Wright, T. J., B. E. Parsons, and Z. Lu. 2004. Toward mapping surface deformation in three dimensions using InSAR. *Geophysical Research Letters*, 31.
- Wu, W.-Y., M.-H. Lo, Y. Wada, J. S. Famiglietti, J. T. Reager, P. J.-F. Yeh, A. Ducharme, and Z.-L. Yang. 2020. Divergent effects of climate change on future groundwater availability in key mid-latitude aquifers. *Nature communications*, 11: 1-9.
- Xiang, L., H. Wang, H. Steffen, P. Wu, L. Jia, L. Jiang, and Q. Shen. 2016. Groundwater storage changes in the Tibetan Plateau and adjacent areas revealed from GRACE satellite gravity data. *Earth and Planetary Science Letters*, 449: 228-239.
- Yang, Y.-J., C. Hwang, W.-C. Hung, T. Fuhrmann, Y.-A. Chen, and S.-H. Wei. 2019. Surface deformation from Sentinel-1A InSAR: relation to seasonal groundwater extraction and rainfall in Central Taiwan. *Remote Sensing*, 11: 2817.
- Zebker, H. A., and J. Villasenor. 1992. Decorrelation in interferometric radar echoes. *IEEE Transactions on geoscience and remote sensing*, 30: 950-959.
- Zebker, H. A., C. L. Werner, P. A. Rosen, and S. Hensley. 1994. Accuracy of topographic maps derived from ERS-1 interferometric radar. *IEEE transactions on Geoscience and Remote Sensing*, 32: 823-836.
- Zhang, C., W. Li, and D. Travis. 2007. Gaps-fill of SLC-off Landsat ETM+ satellite image using a geostatistical approach. *International Journal of Remote Sensing*, 28: 5103-5122.
- Zhang, J., and K. Nawata. 2017. A comparative study on predicting influenza outbreaks. *Bioscience trends*.

Appendix





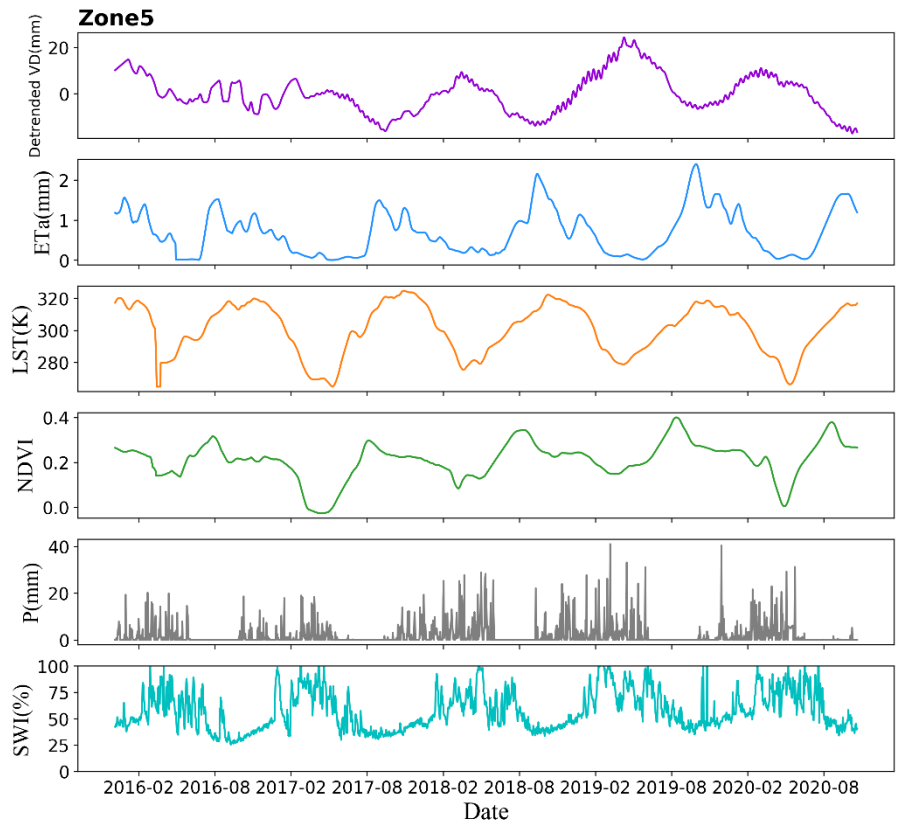


Figure S1. Average values at each date for each variable in Zone 2, 3, 4, and 5. Time shifts for five variables (ETa, LST, NDVI, P, and SWI) were applied. The purple line represents detrended mean displacement rates. The blue line indicates the actual evapotranspiration (ETa) time series. The yellow line denotes land surface temperature (LST) time series. The green line corresponds to NDVI measurements. The black line stands for precipitation time series. The cyan line represents soil water index (SWI).